

NASA/TM-2014-218267



Nonlinear Aeroelastic Analysis of the HIAD TPS Coupon in the NASA 8' High Temperature Tunnel: Theory and Experiment

Benjamin D. Goldman
Duke University, Durham, North Carolina

Robert C. Scott
Langley Research Center, Hampton, Virginia

Earl H. Dowell
Duke University, Durham, North Carolina

NASA STI Program . . . in Profile

Since its founding, NASA has been dedicated to the advancement of aeronautics and space science. The NASA scientific and technical information (STI) program plays a key part in helping NASA maintain this important role.

The NASA STI program operates under the auspices of the Agency Chief Information Officer. It collects, organizes, provides for archiving, and disseminates NASA's STI. The NASA STI program provides access to the NASA Aeronautics and Space Database and its public interface, the NASA Technical Report Server, thus providing one of the largest collections of aeronautical and space science STI in the world. Results are published in both non-NASA channels and by NASA in the NASA STI Report Series, which includes the following report types:

- **TECHNICAL PUBLICATION.** Reports of completed research or a major significant phase of research that present the results of NASA Programs and include extensive data or theoretical analysis. Includes compilations of significant scientific and technical data and information deemed to be of continuing reference value. NASA counterpart of peer-reviewed formal professional papers, but having less stringent limitations on manuscript length and extent of graphic presentations.
- **TECHNICAL MEMORANDUM.** Scientific and technical findings that are preliminary or of specialized interest, e.g., quick release reports, working papers, and bibliographies that contain minimal annotation. Does not contain extensive analysis.
- **CONTRACTOR REPORT.** Scientific and technical findings by NASA-sponsored contractors and grantees.

- **CONFERENCE PUBLICATION.** Collected papers from scientific and technical conferences, symposia, seminars, or other meetings sponsored or co-sponsored by NASA.
- **SPECIAL PUBLICATION.** Scientific, technical, or historical information from NASA programs, projects, and missions, often concerned with subjects having substantial public interest.
- **TECHNICAL TRANSLATION.** English-language translations of foreign scientific and technical material pertinent to NASA's mission.

Specialized services also include organizing and publishing research results, distributing specialized research announcements and feeds, providing information desk and personal search support, and enabling data exchange services.

For more information about the NASA STI program, see the following:

- Access the NASA STI program home page at <http://www.sti.nasa.gov>
- E-mail your question to help@sti.nasa.gov
- Fax your question to the NASA STI Information Desk at 443-757-5803
- Phone the NASA STI Information Desk at 443-757-5802
- Write to:
STI Information Desk
NASA Center for AeroSpace Information
7115 Standard Drive
Hanover, MD 21076-1320

NASA/TM-2014-218267



Nonlinear Aeroelastic Analysis of the HIAD TPS Coupon in the NASA 8' High Temperature Tunnel: Theory and Experiment

Benjamin D. Goldman
Duke University, Durham, North Carolina

Robert C. Scott
Langley Research Center, Hampton, Virginia

Earl H. Dowell
Duke University, Durham, North Carolina

National Aeronautics and
Space Administration

Langley Research Center
Hampton, Virginia 23681-2199

May 2014

Acknowledgments

The authors would first like to thank Christopher M. Little and Dr. Justin D. Littell for coordinating the experimental efforts and bringing the knowledge and tools necessary to collect essential test data. We also acknowledge the valuable input of Walter E. Bruce, Dr. Robert E. Bartels, Dr. Anthony M. Calomino, Dr. F. McNeil Cheatwood, Stephen J. Hughes, Scott C. Splinter, Dr. Alireza Mazaheri, Carrie M. Rhoades, and the 8' HTT wind tunnel technicians.

The use of trademarks or names of manufacturers in this report is for accurate reporting and does not constitute an official endorsement, either expressed or implied, of such products or manufacturers by the National Aeronautics and Space Administration.

Filename: TP-TM1col5
Directory: C:\Users\wbaize\Desktop
Template: C:\Users\wbaize\AppData\Roaming\Microsoft\Templates\Normal.dotm
Title: NASA Technical Memorandum 0000
Subject:
Author: TechPubs
Keywords:
Comments:
Creation Date: 4/10/2014 12:48:00 PM
Change Number: 18
Last Saved On: 6/6/2014 2:08:00 PM
Last Saved By: Baize, Wanda M Hickson (LARC-B702)[LAMPS]
Total Editing Time: 167 Minutes
Last Printed On: 6/10/2014 7:16:00 AM
As of Last Complete Printing
Number of Pages: 4
Number of Words: 573
Number of Characters: 3,775 (approx.)

Abstract

The purpose of this work is to develop a set of theoretical and experimental techniques to characterize the aeroelasticity of the thermal protection system (TPS) on the NASA Hypersonic Inflatable Aerodynamic Decelerator (HIAD). A square TPS coupon experiences trailing edge oscillatory behavior during experimental testing in the 8' High Temperature Tunnel (HTT), which may indicate the presence of aeroelastic flutter. Several theoretical aeroelastic models have been developed, each corresponding to a different experimental test configuration. Von Karman large deflection theory is used for the plate-like components of the TPS, along with piston theory for the aerodynamics. The constraints between the individual TPS layers and the presence of a uni-directional foundation at the back of the coupon are included by developing the necessary energy expressions and using the Rayleigh Ritz method to derive the nonlinear equations of motion. Free vibrations and limit cycle oscillations are computed and the frequencies and amplitudes are compared with accelerometer and photogrammetry data from the experiments.

Contents

1	Introduction	3
2	Test Articles	4
2.1	TPS Coupon	4
2.2	Simplified test article	5
2.3	TPS Material properties	6
3	Experimental apparatus and methods	7
3.1	Mounting fixture	7
3.2	Ground vibration testing (GVT)	9
3.3	Wind tunnel testing	10
4	Theoretical models	11
4.1	Overview of models	12
4.2	Aeroelastic equations of motion and computational methods	14
4.3	Theoretical test cases	17
5	Results	18
5.1	Theoretical and experimental test cases	19
5.2	Theoretical and experimental impulse response	19
5.2.1	Model A and tunnel run 30	20
5.2.2	Model B and tunnel run 30	20
5.2.3	Model C and tunnel run 31	21
5.2.4	Model D and tunnel runs 22 and 23	22
5.3	Theoretical and experimental aeroelastic response	24
5.3.1	Model A and tunnel run 30 at 5° angle of attack	24
5.3.2	Model B and tunnel run 30 at 5° angle of attack	25
5.3.3	Model C and tunnel run 31 at 5° angle of attack	27
5.3.4	Model D and tunnel runs 22, 23 at 2.5° , 5° angle of attack	28
6	Preliminary analysis of in-flight stability	35
7	Concluding Remarks	37
	Appendix	39

1 Introduction

The NASA Hypersonic Inflatable Aerodynamic Decelerator (HIAD) [1] is an inflatable aeroshell with a diameter significantly larger than that of current rigid aeroshells. Its size is not limited by the launch vehicle shroud, allowing heavier payloads to be delivered to higher elevations of planets like Mars. The HIAD is composed of two separate but interacting structural components: a stacked inflatable toroid base structure and a thermal protection system (TPS). The TPS is flexible enough to be packed into a small volume for transport and expands with the inflation of the toroid base structure in space. To evaluate aerothermal performance of this system, a series of experimental tests [2][3] on small TPS coupons in the NASA 8' High Temperature Tunnel (HTT) were conducted. Observations of oscillatory motion and failure of these samples during testing suggested that aeroelastic effects needed additional quantification, and theoretical model development was required. Previous theoretical research by Scott et al.[4] in the NASA Aeroelasticity Branch indicated that thin, flexible membrane structures like the TPS are prone to aeroelastic instabilities which could lead to failure. Several works by Dowell [5][6] studied similar instabilities for panel structures in supersonic flow. Goldman and Dowell [7] also developed some preliminary theoretical models for earlier TPS coupon tests. A team comprised of the aforementioned researchers as well as others was formed to study this problem, which is the subject of this paper.

Flexible structures will exhibit instabilities in a wind-tunnel test for several reasons [8][9]. First, resonance may be induced from vibrations of the wind-tunnel itself, a noise source such as a turbulent boundary layer, or from pulsations in the tunnel mean flow pressure. Second, an interaction between the aerodynamic forces and the flexible structure could cause an aeroelastic instability known as “flutter.” Unlike resonance, flutter in supersonic flow is usually due to the coalescence of two natural structural modes, and a bifurcation resulting in a state of zero system damping. Nonlinearities in the structural materials may cause limited amplitude flutter or “limit cycle oscillations” (LCOs). Repeated cycles of these oscillations will fatigue the material and may result in failure. Based on the local Mach number and dynamic pressure in the 8' HTT along with some preliminary theoretical predictions, it was determined that the flutter boundary of the TPS coupon in the tunnel had been exceeded and flutter in the form of LCO was likely to be the predominant source of oscillations.

We emphasize that observation of TPS coupon flutter in the 8' HTT does not necessarily imply that the TPS attached to the HIAD will exhibit instability in flight. The likelihood of a structure to encounter flutter is especially dependent on the local flow parameters (Mach number and dynamic pressure). CFD simulations [10] of a proposed HIAD re-entry trajectory indicate that the local flow conditions on the vehicle surface are significantly less severe than those in the tunnel. It has also been observed [11] in some experimental testing of inflatable aerodynamic decelerators that a substantial static pressure differential compresses the outer TPS layer between the valleys of the inflated base structural members. It is well known that increasing the static pressure differential across plate and shell systems also rapidly increases the flutter boundary, due to the induced tension from static deformation. Other key factors in aeroelastic stability are the structural geometry and boundary conditions. While the TPS coupon is a square with (relatively) supported boundaries, the TPS on the HIAD structure is a large truncated conical shell with less traditional boundary conditions. The aeroelastic behavior of these two structures may be significantly different, so it

is necessary to evaluate both cases before making in-flight predictions. Some preliminary analysis of in-flight stability is provided at the end of this report, which is based on the local geometric similarities between the TPS coupon in the tunnel and the in-flight configuration.

The main focus of this work will be to calculate and analyze theoretical limit cycle oscillations for all TPS test configurations in the 8' HTT and compare with the experimental results. Accelerometers, high speed imaging, and photogrammetry will be used to collect most of the experimental data. The oscillation amplitudes and frequencies will be used as the two main comparison parameters. However, similar frequency content between a theoretical flutter solution and the experiment does not conclusively indicate that flutter is the sole oscillation mechanism. A substantial effort will also be made to characterize free vibrations, using both theoretical and experimental impulse response tests. Tunnel vibrations or flow pressure resonant excitation can then be ruled out if and when data from those sources is available.

2 Test Articles

2.1 TPS Coupon

The 1st generation TPS coupon [3], illustrated in Figure 1, consists of one layer of Aluminized Kapton Kevlar (AKK), four layers of Pyrogel 2250, and two layers of Nextel 440-BF20. The two Nextel layers are stitched together in various diamond patterns, along with tacks at certain point-wise locations that constrain all of the layers together. The coupon arrives from the manufacturer as shown in Figure 2. Black dots are painted on the outermost Nextel layer for the purpose of photogrammetry, and the extra material (tabs) at the edges are stitched with Velcro and used to restrain the sample during testing. The nominal size of the sample, excluding the Velcro tabs, is 2' x 2'.

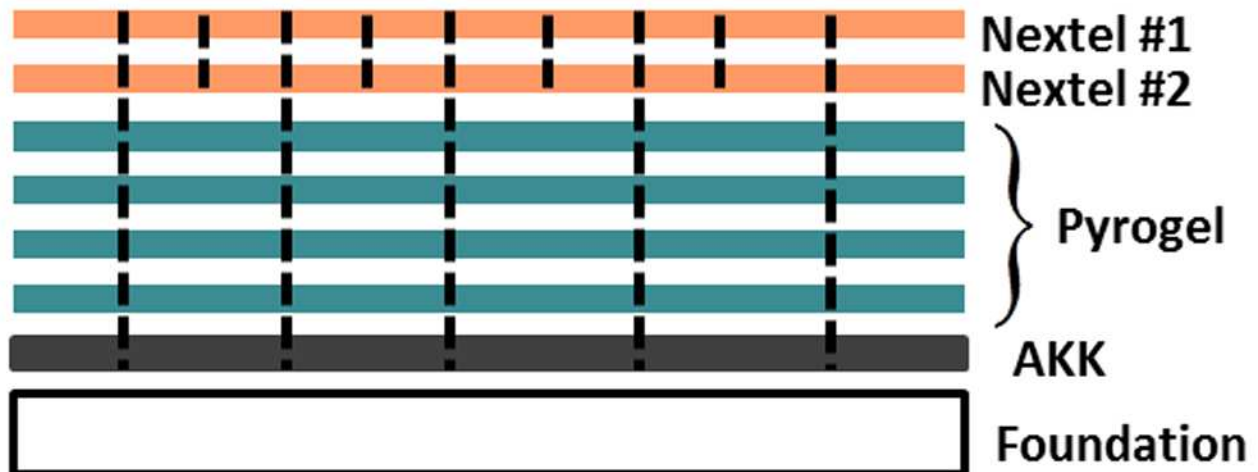


Figure 1: TPS layup consisting of 2 x Nextel 440 BF-20, 4 x Pyrogel 2250, and 1 x AKK.

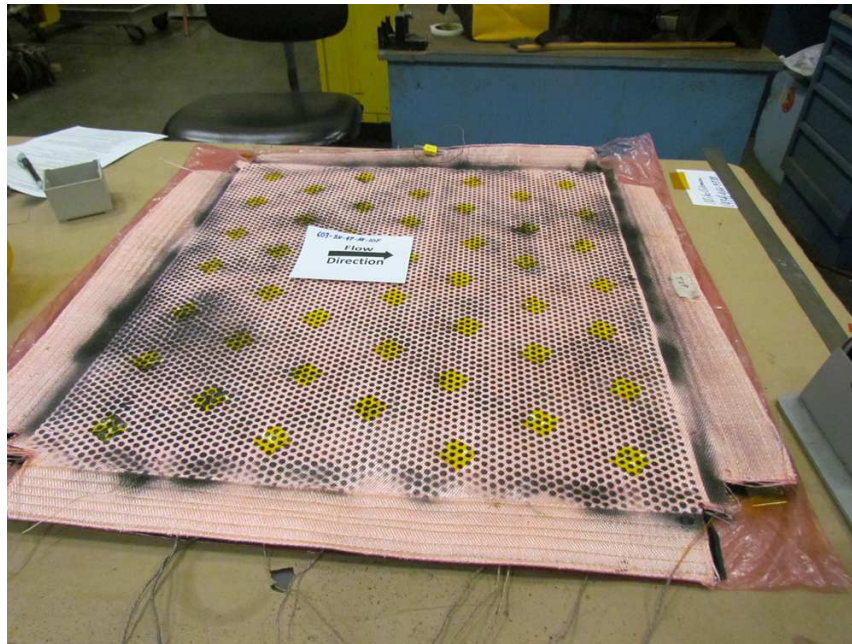


Figure 2: TPS coupon as arrived from manufacturer, with painted photogrammetry dots.

2.2 Simplified test article

In addition to the TPS coupon, a simplified test article of the same size was developed specifically for aeroelastic analysis, since the multiple layer TPS coupons are complex, non-traditional aeroelastic systems. The simplified article, shown in Figure 3, consists of two layers of Nextel and one layer of AKK, stitched together in a dense 2" square pattern to form a single panel-like structure. It is necessary to have all three layers connected together to limit heating of the instrumentation on the back side of the sample and to prevent hot gas from damaging vital tunnel infrastructure. The stitch density is high enough to ensure the sample behaves as a single continuous layer. Figure 4 shows the back side of the article, where the stitching is sealed with Kapton tape to prevent any possible flow penetration. Also shown are the Velcro tabs at the edges also used to secure the sample during testing.

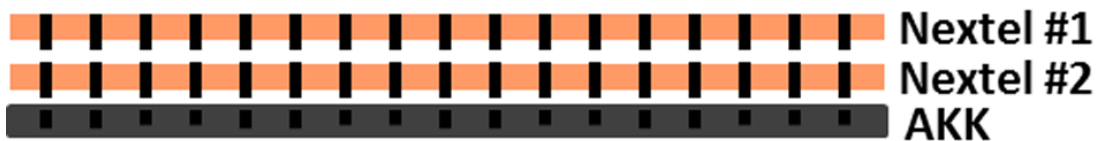


Figure 3: Simplified test article material configuration, consisting of 2 x Nextel 440-BF20 and 1 x AKK.



Figure 4: Back side of the simplified test article with attached thermocouple, accelerometer, and Velcro tabs.

2.3 TPS Material properties

Material properties needed for a theoretical aeroelastic evaluation are given in Table 1. The Young's moduli and Poisson ratios of the individual layers were obtained from material documentation (see citations in Table 1), while thickness, mass, and the effective bending stiffness were measured experimentally. The bending stiffness was measured by performing impulse-response ground vibration tests of tension-free material layers draped over an open cavity mounting fixture. This procedure is detailed in subsection 3.2. The experimental natural frequency spectrum for a known input force was compared to the spectrum calculated using nonlinear theory for a given value of bending stiffness, until the best agreement between theory and experiment was achieved. The results for the simplified test article are shown in Figure 17a in section 5.2.4.

Note that the Young's modulus of the simplified test article is unknown because the three layers stitched together behave differently in-plane than a single layer alone. When comparing to the experimental results, the Young's modulus will be a free parameter that can be adjusted for best agreement between experiment and theory.

Material	Young's Modulus E (Pa)	Poisson's Ratio ν	Mass/area m (kg/m^2)	Bending stiffness D (Pa m^3)	Spring stiffness k (Pa/m)
Nextel 440-BF20	1.9e11 [12] (fibers)	0.26 [13]	0.46	0.5	N/A
Aluminized Kapton Kevlar (AKK)	1.24e11 [14] (Kevlar 49 fibers)	0.36 [15]	0.14	0.5	N/A
Pyrogel 2250	3e6 [16] (Silica Aerogel)	0.20 [16]	1.36	N/A	3.9e7 (4 layers)
Simplified Test Article	from experiment	0.30 (est)	1.83	5	N/A

Table 1: Material properties of the individual TPS layers and simplified test article.

3 Experimental apparatus and methods

3.1 Mounting fixture

Prior to experimental testing, the samples are secured to a metal fixture in various configurations. The main fixture consists of a (vented) open cavity, shown in Figure 5. While the simplified test articles and individual layers are tested in this configuration, the TPS coupons are tested on either a flat, rigid foundation or on a toroid simulator. In these cases, the open cavity is modified using either of the two foundation inserts shown in Figure 6. There are no restraints that hold the coupon to the surfaces of the foundations other than at the edges, so the coupon middle surface is allowed to lift off the foundations at any time during testing.

The test samples are secured to the fixture via a system of rectangular metal plates that have Velcro strips embedded. The plates are then compressed against the opposing Velcro tabs at the four edges of the test samples, to form a secure connection. The plates are connected to eight washer stacks on the fixture via brackets (two on each side), which can be compressed with bolts, thus securing the sample to the fixture. Additional compression of the washer stacks enable known amounts of bi-axial tension to be applied, since calibrations have been performed based on the washer stack compression distance. In the case of the TPS coupon, the metal plates are connected only to the AKK layer, since it is the structural load-carrying component of the TPS. The Nextel is allowed to “float” on the other layers with minimal tension by folding over its Velcro tabs only after the AKK has been tensioned. A TPS coupon in this configuration is shown in Figure 7. The simplified test article is mounted in a similar fashion, except that the entire sample is tensioned, since it cannot be separated into individual layers.



Figure 5: Open cavity mounting fixture



(a) Flat foundation.



(b) Toroid foundation.

Figure 6: Flat and toroid foundation inserts for the mounting fixture.

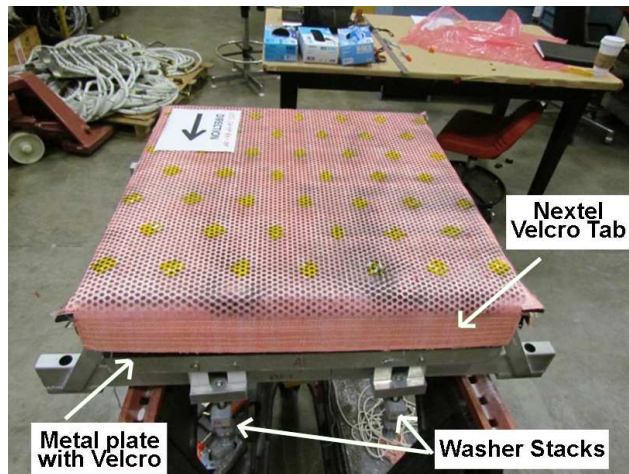


Figure 7: TPS coupon tensioned over the mounting fixture.

3.2 Ground vibration testing (GVT)

The purpose of ground vibration testing (GVT) is to determine experimentally the natural modes and natural frequencies of the sample. Due to the complexity of the foundations and time constraints, only the natural frequencies of the samples are recorded. For GVTs of the TPS coupon, two accelerometers and a transducer hammer are connected to a Bruel and Kjaer Pulse system. One accelerometer is attached to the outermost Nextel layer, and the other accelerometer is attached to the bottom of the AKK, at the same middle surface location. This allows one to distinguish between the Nextel and AKK responses at a given point. When the coupon is mounted on the rigid foundation, a small hole is made to prevent impingement of the AKK accelerometer. The transducer hammer, shown in Figure 8, is used to impact the sample at various locations along its surface, and FFTs as well as the hammer impact forces are recorded. The response is heavily dependent on the location of excitation, so the sample is divided into quadrants and response is measured for a hammer impulse in each quadrant. Impulses at some locations excite only one or two modes, while impulses at other locations resulted in excitation of several modes. GVTs are performed on the TPS coupon on both flat and toroid foundations immediately before tunnel testing, with and without applied tension in the AKK, and mounted both in and out of the tunnel sled (Figure 9). The tunnel sled impinges on the outer Nextel, adding additional tension. However, this added tension relaxes after the tunnel air is turned on, so in-tunnel GVTs of the TPS coupon are not analyzed in this report. For brevity, only pre-run, tensioned, out-of-tunnel sled GVTs will be compared directly to theoretical predictions.

For the simplified test article, GVTs are performed on the open cavity fixture, with and without tension, in and out of the tunnel sled, and pre- and post-tunnel run. The un-tensioned GVT allows the bending stiffness to be inferred from the frequency response, and the tensioned GVT allows verification of tension formulation in the theoretical model. Since the simplified test article is much thinner than the TPS coupon, the tunnel sled no longer impinges on the edges of the sample, so there is no difference in response for GVTs in and out of the tunnel sled. GVTs are performed before and after running the tunnel to help characterize how much tension had relaxed from the sample during the test. Note that in this case, the data collection system in the tunnel is used to record accelerometer response from the GVT instead of the Pulse system.

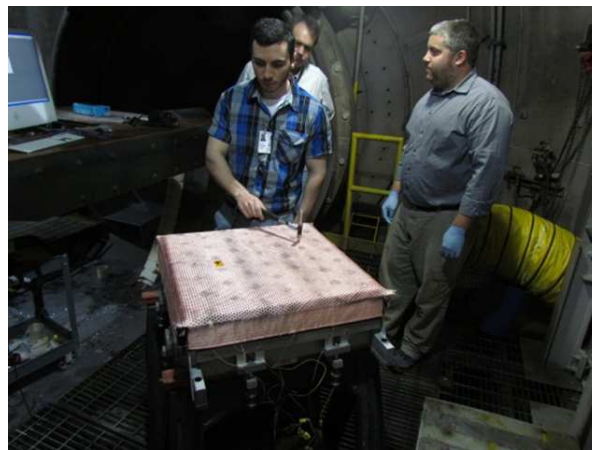


Figure 8: Hammer impact of the TPS coupon during GVT.

3.3 Wind tunnel testing

Wind tunnel tests are conducted in the NASA 8' High Temperature Tunnel (HTT) with the (free-stream) Mach 6.7 nozzle [17]. The samples are mounted in a sled, shown in Figure 9, which is placed in the flow at a desired angle of attack. The angle of attack corresponds to a specific local Mach number and dynamic pressure, as given in Table 2. The free stream Mach number and dynamic pressure in the 8' HTT are fixed for a selected nozzle, so only the sled angle of attack can change the local flow parameters (they cannot be varied independently). Samples cannot be tested at zero degrees angle of attack due to the effects from a shock that forms at the sled leading edge. The tunnel run time is also limited to a maximum of 90 seconds, since the compressed air and liquid oxygen needed for a single run are stored in a bottle farm with a fixed capacity.

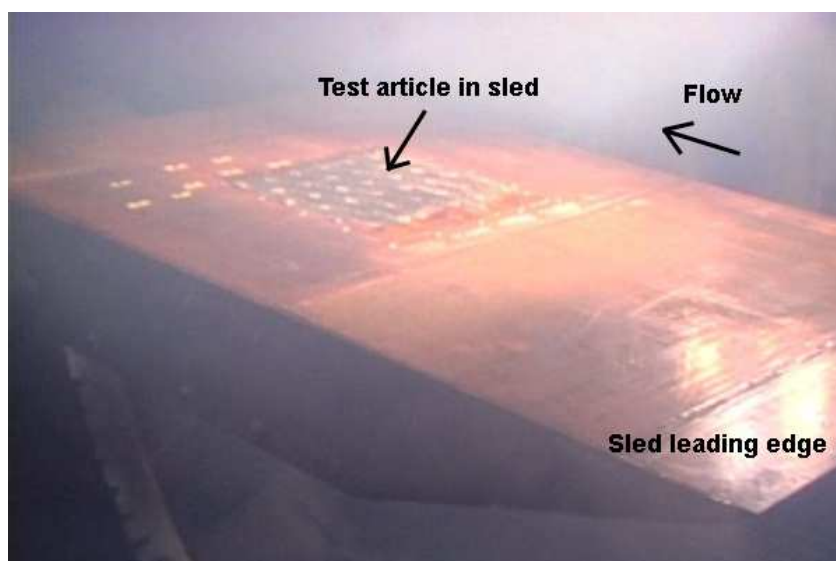


Figure 9: TPS coupon mounted in the 8' HTT sled at 5° angle of attack.

Angle of attack (degrees)	Local Mach number	Dynamic pressure (Pa, psf)	
0	5.8	33,094	691
2.5	5.6	46,884	979
5	5.35	60,763	1,270
7.5	5.1	74,463	1,555
10	4.8	88,252	1,843

Table 2: Local sled Mach number and dynamic pressure in the 8' HTT as a function of angle of attack.

The ongoing experimental testing of the TPS coupon had focused on thermal response mea-

surements with no instrumentation for aeroelastic analyses. Two specific runs from the scheduled HIAD TPS coupon test matrix, identified as runs 30 and 31, were selected for aeroelastic analysis. The samples in both runs are identical in terms of stitching pattern and applied tension, but one is mounted on a flat, rigid foundation (run 30), while the other is mounted on a toroid foundation (run 31). During aeroelastic testing, the Nextel accelerometer is removed since it would be destroyed in the high temperature flow. Instead, photogrammetry is used to measure the time dependent amplitude of the outermost Nextel layer, though the data sample rate is usually insufficient for frequency response measurements. The photogrammetry analysis is elaborate and not included in this paper, but additional detail for a similar procedure can be found in [18]. The accelerometer is left on the back of the AKK and is the primary measure of frequency response during the test. It is positioned 5 inches behind the trailing edge, since that is where most deflection is seen during testing. For these tests, the tunnel runs for 90 seconds or until the sample fails.

The tests for the simplified test article are identified in the scheduled TPS test matrix as runs 22 and 23 (Note that these runs were performed after TPS runs 31 and 32. The run numbering corresponds to the available openings in the TPS test matrix, originally organized by the HIAD FTFS team). Two identical samples were constructed and outfitted with thermocouples and accelerometers on the bottom AKK layer. The foundations were removed from the fixture to leave an open cavity for the tunnel runs. Since the insulator (Pyrogel) is no longer present in these samples, heating of the instrumentation and degradation of the AKK is possible unless the tunnel run time is reduced considerably. For these tests, the total time exposed to the flow is eight seconds. A summary of the tunnel tests considered in this report is given in table 3.

Run	Sample	Stitching	Angle of attack (deg)	Foundation
22	Simplified test article	Dense 2" squares thru all layers	5 - 2.5	Open cavity
23	Simplified test article	Dense 2" squares thru all layers	2.5 - 5	Open cavity
30	TPS coupon	60° diamond quilting, 3" spacing	5	Flat
31	TPS coupon	60° diamond quilting, 3" spacing	5	Toroid

Table 3: Experimental tunnel runs considered for aeroelastic analysis.

4 Theoretical models

In this section, structural models of the TPS coupon and simplified test article are introduced. The first three models, A, B, and C, correspond to the TPS coupon, while model D corresponds to the simplified test article. The aeroelastic equations of motion are then developed for the most elaborate models, and numerical solution methods are discussed. A table outlining all of the theoretical results is also provided.

4.1 Overview of models

Structural models of the TPS coupon are based on physical inspection as well as on the properties of the individual materials. The Nextel and AKK layers are sufficiently rigid to be approximated as plates, while the Pyrogel is a sponge-like layer that contributes inertia (when appropriate) and spring stiffness but has negligible bending rigidity. Bi-axial tension can be applied to all layers; however, it is only applied directly to the AKK layer in the experimental coupon tests. The boundary conditions are approximated as simply supported and stress-free for all layers in all test cases. The four different models corresponding to different experimental configurations are shown in Figure 10.

The first theoretical model is the two-layer Pyrogel foundation model (A), shown in Figure 10a, which corresponds to the experimental test on the flat, rigid foundation. In this system, two layers of Nextel stitched to each-other at specified middle surface locations rest on a uni-directional Pyrogel foundation. This foundation is highly nonlinear, in that it has a nominal spring stiffness in compression but it has zero spring stiffness in tension. This effectively allows the layers to lift off the foundation at any time during the simulation (note: the boundaries are still restrained). The AKK layer is not included in this model.

The three-layer rigid foundation model (B) in Figure 10b also corresponds to the experimental test on the flat, rigid foundation, but it includes the AKK layer which is stitched to the Nextels at specified middle surface locations. The Pyrogel is no longer a foundation but rather a linear spring-layer that is sandwiched between the second layer of Nextel and the AKK. The AKK then rests on a uni-directional spring foundation that is significantly more rigid than the Pyrogel, which simulates the presence of the rigid ceramic foundation under the sample. As before, this foundation enables the entire sample to lift off during the simulation.

The three-layer toroid foundation model (C) in Figure 10c corresponds to the experimental test on the toroid foundation. It is similar to model B except that the rigid foundation is truncated in the stream-wise direction to match the dimensions of the relatively flat portion of the aluminum toroid in Figure 6b. The curvature of the toroid is not accounted for, so it can be thought of as a flat bar running underneath the coupon that does not impart any stiffness in tension, but has high stiffness in compression. Additionally, a static pressure differential may be imposed in this model, allowing the TPS material to statically deform on either side of the toroid.

The single-layer model (D) in Figure 10d corresponds to the experimental single-layer article on the open cavity. This simple theoretical model consists of a single plate without any foundation or middle surface supports, which effectively simulates the open, vented cavity in the experiment. Substantial bi-axial tension may be applied, as well as a static pressure differential.

Finally, the aeroelastic systems are constructed by adding piston theory aerodynamics as an external force to each of the structural models. This linear theory assumes that the aerodynamic pressure is due to the local deflection of the material surface. No shear, skin-friction, or other viscous effects are included. These additional effects may be considered later if necessary.

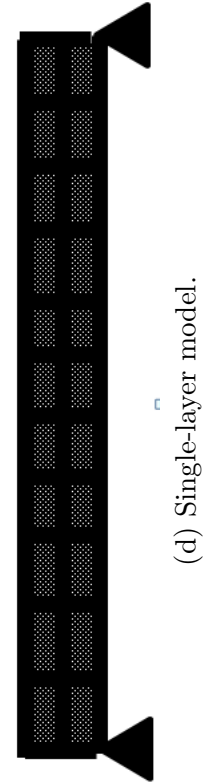
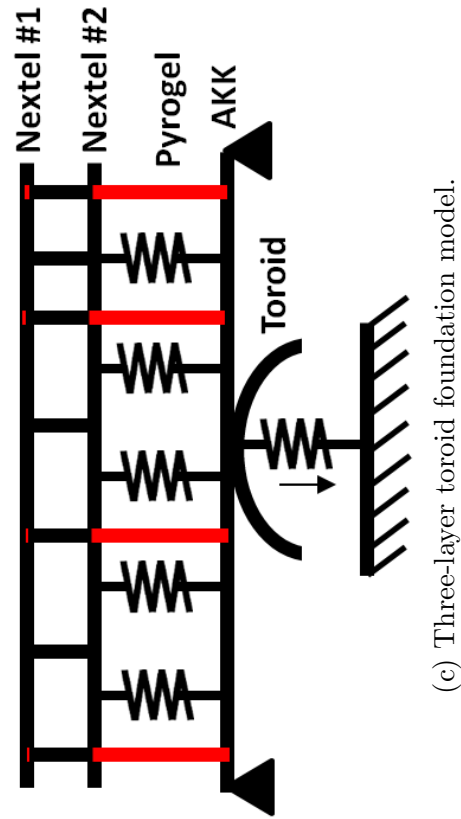
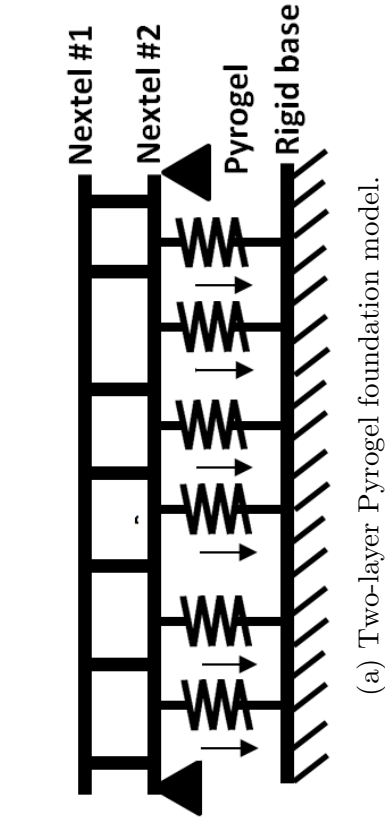
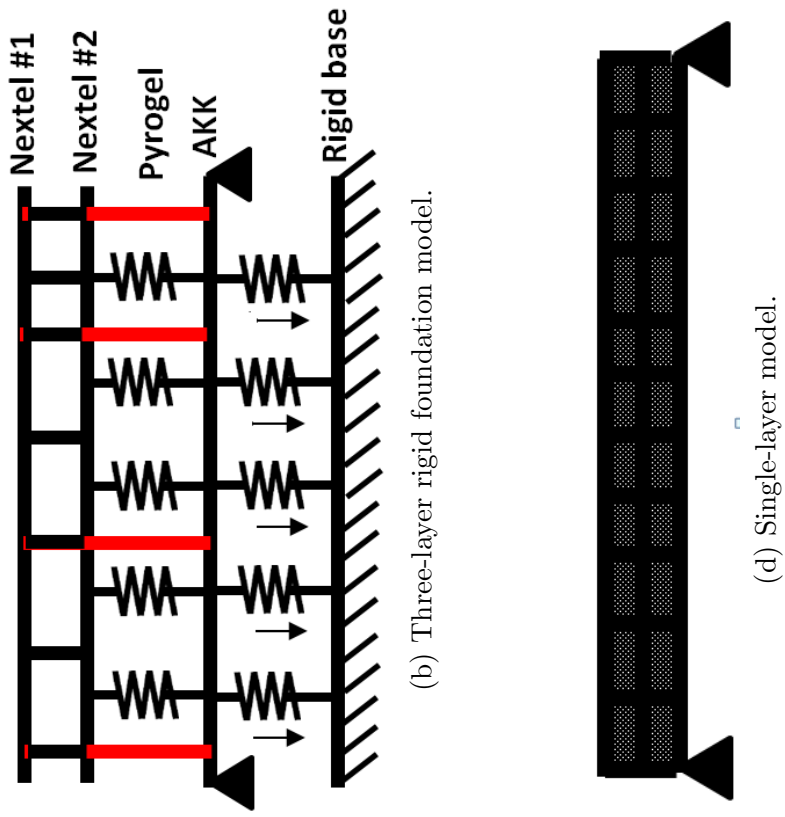


Figure 10: Theoretical structural models of the TPS coupon and simplified test article.

Symbol notes: The downward pointing arrows next to a spring symbol indicates that it is uni-directional. Solid black vertical lines indicate stitching between only the two Nextel layers, and solid red vertical lines indicate stitching between the second Nextel layer and the AKK.

4.2 Aeroelastic equations of motion and computational methods

The Raleigh-Ritz method is used to derive the equations of motion for all of the theoretical models. The formulation provided here will apply to the three-layer rigid and toroid foundation models, since they are the most complex systems. The simpler two-layer and single-layer models can be easily derived using the same method and eliminating the terms for the additional layers and constraints. The modal equations of motion for all four models are provided in the appendix. The total potential energy of the system is:

$$U_{tot} = U_B^{N1} + U_B^{N2} + U_B^K + U_S^{N1} + U_S^{N2} + U_S^K + U^{Pyr} + U^{St} + U^{Fd/Tor} \quad (1)$$

where the subscript B indicates bending energy, subscript S indicates stretching energy, superscript $N1$ is the outer layer of Nextel, superscript $N2$ is the second layer of Nextel, superscript K is the AKK, superscript Pyr is the Pyrogel, superscript St is the stitching, and superscript Fd/Tor is the rigid or toroid foundation. The bending and stretching energies given by von Karman large deflection theory for a **single plate layer** are [6]:

$$U_B = \frac{D}{2} \int_0^b \int_0^a \left\{ \left(\frac{\partial^2 w}{\partial x^2} \right)^2 + \left(\frac{\partial^2 w}{\partial y^2} \right)^2 + 2\nu \frac{\partial^2 w}{\partial x^2} \frac{\partial^2 w}{\partial y^2} + 2(1 - \nu) \left(\frac{\partial^2 w}{\partial x \partial y} \right)^2 \right\} dx dy \quad (2)$$

$$+ \frac{N_x^A}{2} \int_0^b \int_0^a \left(\frac{\partial w}{\partial x} \right)^2 dx dy + \frac{N_y^A}{2} \int_0^b \int_0^a \left(\frac{\partial w}{\partial y} \right)^2 dx dy$$

$$U_S = \frac{1}{2Eh} \int_0^b \int_0^a \left\{ \left(\frac{\partial^2 F}{\partial x^2} \right)^2 + \left(\frac{\partial^2 F}{\partial y^2} \right)^2 - 2\nu \frac{\partial^2 F}{\partial x^2} \frac{\partial^2 F}{\partial y^2} + 2(1 + \nu) \left(\frac{\partial^2 F}{\partial x \partial y} \right)^2 \right\} dx dy \quad (3)$$

where a and b are the sample length and width, D is the bending stiffness, N_x^A is the applied tension in the x-direction, N_y^A is the applied tension in the y-direction, E is the modulus of elasticity, h is the material thickness, ν is the Poisson ratio, w is the out-of plate deflection, and F is the Airy stress function for a given layer. The Airy stress function is defined by:

$$\frac{\partial^2 F}{\partial x^2} = N_y \quad \frac{\partial^2 F}{\partial y^2} = N_x \quad -\frac{\partial^2 F}{\partial x \partial y} = N_{xy} \quad (4)$$

where N_x , N_y , and N_{xy} are the in-plane stress resultants. The potential energy of the Pyrogel (as a linear spring-layer) is:

$$U^{Pyr} = \frac{k^{Pyr}}{2} \int_0^b \int_0^a (w^{N2} - w^K)^2 dx dy \quad (5)$$

where k^{Pyr} is the spring constant of the Pyrogel.

In this formulation, the stitches constraining the layers are simple linear springs with $k^{St} \gg k^{Pyr}$, where k^{St} is the spring constant of the stitch. The stitching energy may take different forms depending on the desired pattern. For point-wise tack locations, the stitching energy may be written

as:

$$U^{St} = \frac{k^{St}}{2} \sum_i (w^{N1} - w^{N2})^2 \Big|_{x_i, y_i} + \frac{k^{St}}{2} \sum_j (w^{N2} - w^K)^2 \Big|_{x_j, y_j} \quad (6)$$

where the first term above represents the point-wise stitching between the two Nextel layers, and the second term represents the point-wise stitching between the Nextels and AKK. The summation indices indicate the number of stitches, and x_i, y_i are the stitch locations. For stitching in lines along the stream-wise direction between the two Nextels, the stitching energy is

$$U^{St} = \frac{k^{St}}{2} \sum_i \int_0^a (w^{N1} - w^{N2})^2 \Big|_{y_i} dx \quad (7)$$

Similarly, stitching in lines along the spanwise direction is:

$$U^{St} = \frac{k^{St}}{2} \sum_i \int_0^b (w^{N1} - w^{N2})^2 \Big|_{x_i} dy \quad (8)$$

Combining expressions (6), (7), and (8) in various ways would allow more complex stitching patterns to be used, but would also require more terms in the modal expansions for deflection.

The potential energy of the uni-directional foundation, with $k^{Fd} \gg k^{Pyr}$ is:

$$U^{Fd} = \frac{k^{Fd}}{2} \int_0^b \int_0^a H[-w^K] (w^K)^2 dx dy \quad (9)$$

Similarly, the potential energy of the toroid foundation is:

$$U^{Tor} = \frac{k^{Tor}}{2} \int_0^b \int_{x_1}^{x_2} H[-w^K] (w^K)^2 dx dy \quad (10)$$

where $H[]$ is the Heaviside step function, and x_1 and x_2 are the start and end locations of the toroid in the stream-wise direction, respectively.

The kinetic energies for all components are given by:

$$\begin{aligned} T^{N1} &= \frac{m^{N1}}{2} \int_0^a \int_0^b \left(\frac{\partial w^{N1}}{\partial t} \right)^2 dx dy \\ T^{N2} &= \frac{m^{N2}}{2} \int_0^a \int_0^b \left(\frac{\partial w^{N2}}{\partial t} \right)^2 dx dy \\ T^K &= \frac{m^K}{2} \int_0^a \int_0^b \left(\frac{\partial w^K}{\partial t} \right)^2 dx dy \\ T^{Pyr} &= \frac{m^{Pyr}}{2} \int_0^a \int_0^b \left(\frac{\partial w^{N2}}{\partial t} + \frac{\partial w^K}{\partial t} \right)^2 dx dy \end{aligned} \quad (11)$$

where m is the mass per area of a given layer.

The Lagrangian of the system is:

$$L = T_{tot} - U_{tot} \quad (12)$$

The virtual work due to aerodynamic loading is:

$$\begin{aligned}
\delta W_{aero}^{N1} &= - \int_0^b \int_0^a \left(\frac{2q}{M} \left[\frac{\partial w^{N1}}{\partial x} + \frac{1}{U_\infty} \frac{\partial w^{N1}}{\partial t} \right] + p_s \right) \delta w dx dy \\
\delta W_{aero}^{N2} &= - \int_0^b \int_0^a \left(\frac{2q}{MU_\infty} \frac{\partial w^{N2}}{\partial t} \right) \delta w dx dy \\
\delta W_{aero}^K &= - \int_0^b \int_0^a \left(\frac{2q}{MU_\infty} \frac{\partial w^K}{\partial t} \right) \delta w dx dy
\end{aligned} \tag{13}$$

where q is the dynamic pressure, M is the Mach number, U_∞ is the free-stream velocity, and p_s is the static pressure differential (The static pressure differential cannot be included when the rigid foundation is used). The aerodynamic pressure is given by the first order Piston theory and is applied only to the outermost Nextel layer (N1), since it is the only layer exposed directly to flow. Since the entire TPS coupon is present in a field of (approximately) uniform density, aerodynamic damping is included in the virtual work for all layers.

In the experimental free vibration analysis, a force impulse is applied to a point on the sample via a transducer hammer. The equivalent theoretical experiment can be formulated using the virtual work due to an applied point-force at an instant in time:

$$\delta W_{hammer}^{N1} = -\delta(t - t_o) F_{app} \delta w^{N1} \Big|_{x_o, y_o} \tag{14}$$

where δ is the Dirac delta-function, F_{app} is the applied force magnitude, and x_o and y_o are the coordinates of the location where the hammer is applied. The force is only applied to the outermost Nextel layer, since the Pyrogel spring layer and stitch constraints transmit the force to the other layers in the sample.

Next, the deflection and stress function of each layer are expanded using assumed natural modes that satisfy the boundary conditions. The boundary conditions are approximated as:

$$\begin{aligned}
w = 0, \quad \frac{\partial^2 w}{\partial x^2} = 0, \quad N_x = 0 \Big|_{x=0, a} \\
w = 0, \quad \frac{\partial^2 w}{\partial y^2} = 0, \quad N_y = 0 \Big|_{y=0, b}
\end{aligned} \tag{15}$$

In this case, the sample is assumed to have simply-supported edges. The axial stress due to the deflection of the layers is assumed to vanish at the edges since no in-plane restraints exist. Note that by the principle of superposition, the static applied in-plane loads are considered in the bending energy and are not included in the stress function. The modal expansions for the deflections and stress functions are:

$$\begin{aligned}
[w^{N1}, w^{N2}, w^K] &= \sum_n \sum_m [a_{nm}(t), b_{nm}(t), c_{nm}(t)] \phi_{nm}(x, y) \\
[F^{N1}, F^{N2}, F^K] &= [F_h^{N1}, F_h^{N2}, F_h^K] + \sum_n \sum_m [d_{nm}(t), e_{nm}(t), f_{nm}(t)] \phi_{nm}(x, y)
\end{aligned} \tag{16}$$

where ϕ_{nm} is the modeshape function. Two indices are used to specify the mode number in both the x and y directions. In this case, it is insufficient to retain one span-wise mode due to the

nonlinearities that arise from the uni-directional foundations. The stress function expansions contain homogeneous solutions F_h and particular solutions (modal series). The homogeneous solutions satisfy:

$$\nabla^4 F = 0 \quad (17)$$

For stress-free boundaries the homogeneous solutions vanish. The particular solutions are found by solving the equation of strain compatibility for plates [5]:

$$\frac{\nabla^4 F}{Eh} = \left(\frac{\partial^2 w}{\partial x \partial y} \right)^2 - \frac{\partial^2 w}{\partial x^2} \frac{\partial^2 w}{\partial y^2} \quad (18)$$

A compatibility relation is written for each layer, and a Galerkin approach is used to find an integral average solution for the stress function modal coordinates (d_{nm}, e_{nm}, f_{nm}) in terms of the deflection coordinates (a_{nm}, b_{nm}, c_{nm}) . The Lagrangian is then written in terms of deflection coordinates only, and the Lagrange equation of the following form is applied:

$$\frac{d}{dt} \left(\frac{\partial L}{\partial \dot{q}_n} \right) - \frac{\partial L}{\partial q_n} + Q_n = 0 \quad (19)$$

The generalized forces Q_n are related to the virtual work by the relation:

$$\delta W = - \sum_n Q_n \delta q_n \quad (20)$$

where q_n is the desired deflection coordinate, which can be specified by a single modal index n .

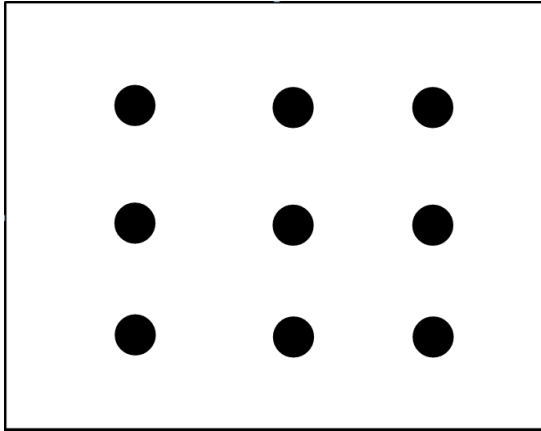
Applying the procedure above results in a nonlinear coupled system of modal equations, which are provided in the appendix. The equations are solved using the 4th order Runge-Kutta integration scheme in MATLAB; however, the code must be structured to handle a large number of equations, possibly $O(100)$ for each layer in the TPS. Nested loop summations are highly inefficient and computationally costly. A vectorization procedure has been developed to remedy this problem and is discussed in detail in the appendix.

4.3 Theoretical test cases

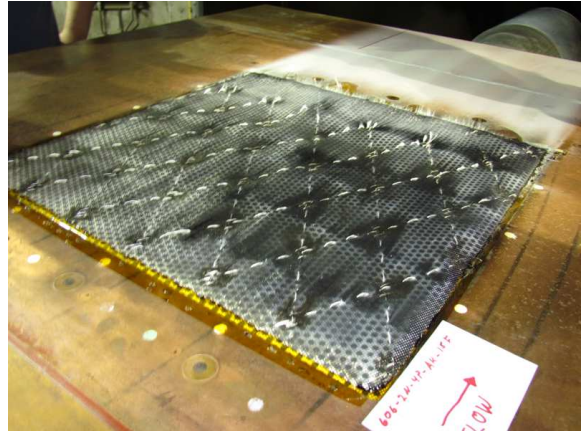
Each theoretical model in Figure 10 has several parameters that can be adjusted to best match the corresponding experiments. For simplicity, the models have been reduced to the theoretical test cases shown in Table 4. The 525 N/m bi-axial tension corresponds to the amount of (approximate) tension that was applied directly to the AKK in the TPS coupon and to the entire simplified test article. The static pressure differential was approximated based on the amount of static deflection seen in the experiments (or eliminated entirely, based on computational restrictions). Note that the static pressure differential for all models is zero for impulse response calculations. The theoretical stitching pattern is 9 tack points that go through all layers, as shown in Figure 11a. This is an approximation of the experimental stitching pattern in Figure 11b. The diamond stitching in Figure 11b only goes through the two layers of Nextel, while the tacks (composed of two Nextel threads) at the intersection points of the diamonds go through all layers. The theoretical 9-point pattern was found to be the optimal initial approximation of the stitching, in that it captures much of the physics of the system, while moderate in computational cost.

Model	Stitching	Angle of attack (deg)	Foundation	Tension	p_s
A	9 tack points	0, 2.5, 5, 7.5, 10	Flat	None	0
B	9 tack points	0, 2.5, 5, 7.5, 10	Flat	525 N/m on AKK	0
C	9 tack points	0, 2.5, 5, 7.5, 10	Toroid	525 N/m on AKK	250
D	9 tack points	0, 2.5, 5, 7.5, 10	None	525 N/m	0 - 250

Table 4: Theoretical test cases.



(a) Theoretical 9-point stitching pattern.



(b) Experimental 60° 3" diamond stitching pattern.

Figure 11: Theoretical and experimental stitching patterns for the TPS coupon.

5 Results

In this section, the selected experimental runs will be compared to the theoretical test cases. Subsection 5.1 will present a summary of the cases in the order in which they will be discussed. In subsection 5.2, the “air-off” results will be compared. This includes theoretical impulse response calculations and the experimental ground vibration tests (GVTs) for each test case. Finally, the aeroelastic response for both theory and experiment will be analyzed in subsection 5.3. In addition, some supplemental calculations on the effect of tension, pressure differential, and foundation for the single-layer model will be presented even though corresponding experimental data are not yet available.

5.1 Theoretical and experimental test cases

The tunnel runs and their corresponding theoretical test cases are given in Table 5. The experimentally applied bi-axial tension is 525 N/m on the AKK for runs 30 and 31, as well as the simplified test article. In the case of impulse response/GVT, the static pressure differential is always zero. We also note that tunnel runs 22 and 23 are the same exact configuration, except that the order in which the angle of attack is prescribed in the tunnel is reversed. The reasoning for this will be discussed in subsection 5.3.4.

Experiment				Theory			
Run	Angle of attack	Stitching	P _o (Pa)	Model	Angle of attack	Stitching	P _o (Pa)
30	5	60°, 3" Diamond	> 0	A & B	0, 2.5, 5, 7.5, 10	9 tack points	0
31	5	60°, 3" Diamond	> 0	C	0, 2.5, 5, 7.5, 10	9 tack points	250
22	5.0 - 2.5	2" square	> 0	D	0, 2.5, 5, 7.5, 10	none	0 - 250
23	2.5 - 5.0	2" square	> 0	D	0, 2.5, 5, 7.5, 10	none	0 - 250

Table 5: Experimental runs and corresponding theoretical test cases.

5.2 Theoretical and experimental impulse response

In this section, the impulse response results are presented for the theoretical and experimental test cases given in Table 5. To properly resolve the stitching constraints in the simulations, 100 terms were retained in the modal expansions for each of the TPS layers. The time required to compute 0.2 seconds of response is on the order of 24 hours. Without vectorization of the code, computations of this type cannot be performed in any reasonable amount of time.

We also observe that the responses in both the GVTs and theoretical impulse response tests calculations change in amplitude and frequency depending on the initial excitation force (hammer/impulse) and the location in which the force is applied. As a result, the experimental parameters such as hammer force, hammer impact location, and accelerometer location were duplicated in the calculations. The hammer impact forces are in the range of 0.001 to 0.005 Newtons depending on the sample. The impact locations resulting in excitation of the maximum number of modes was in any corner of the sample opposite the accelerometer location.

5.2.1 Model A and tunnel run 30

The impulse response for model A and the GVT of the TPS coupon on the rigid foundation in tunnel run 30 are both given in Figure 12. There is generally poor agreement between theory and experiment, although the general trend in response between 100 and 400 Hz is similar. The theory predicts a fundamental natural frequency at 15 Hz, while the fundamental in the experiment is at 60 Hz (there is a possibility of an electronic spike due to interference at 60 Hz, but it is unlikely since this peak is not present in all measurements). It is unclear why there is a discrepancy between theory and experiment, but one possible reason is that the tensioned AKK layer is not present in the theoretical model and therefore cannot contribute any stiffness to the system. It is also very difficult to get consistent experimental response when using hammer impact testing on the rigid foundation, due to the extreme nonlinearity.

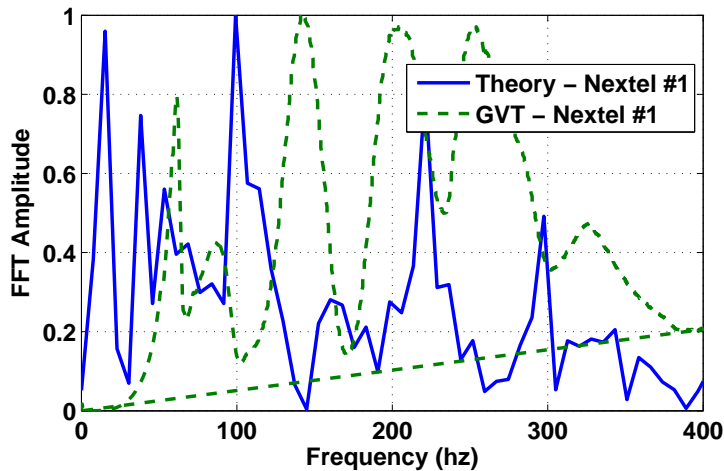


Figure 12: Impulse response for model A and tunnel run 30.

5.2.2 Model B and tunnel run 30

The impulse response for model B and the GVT of the TPS coupon on the rigid foundation in tunnel run 30 are given in Figure 13 for the outer Nextel and in Figure 14 for the AKK. Several key characteristics in these results may indicate the theory is capturing much of the physics in the system. First, in both theory and experiment, the response of the AKK is primarily at the lower modes and response drops off rapidly with increasing frequency. Second, in both theory and experiment, there is significant excitation of several Nextel modes between 50 Hz and 300 Hz, though the frequencies seem to be shifted arbitrarily. Third, in both theory and experiment, there is a rapid drop-off in response above 400 Hz. This is despite the fact that a total of 100 modes were retained in the computations. However, there is still a discrepancy at the fundamental natural mode, where the experimental frequency is significantly higher than that of the theory.

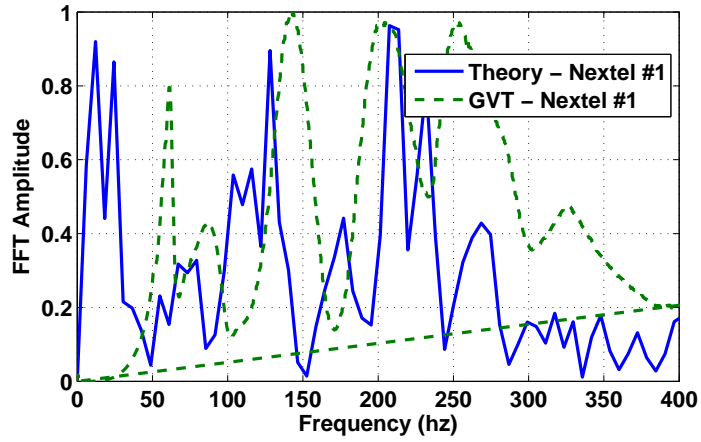


Figure 13: Impulse response of Nextel #1 in model B and tunnel run 30.

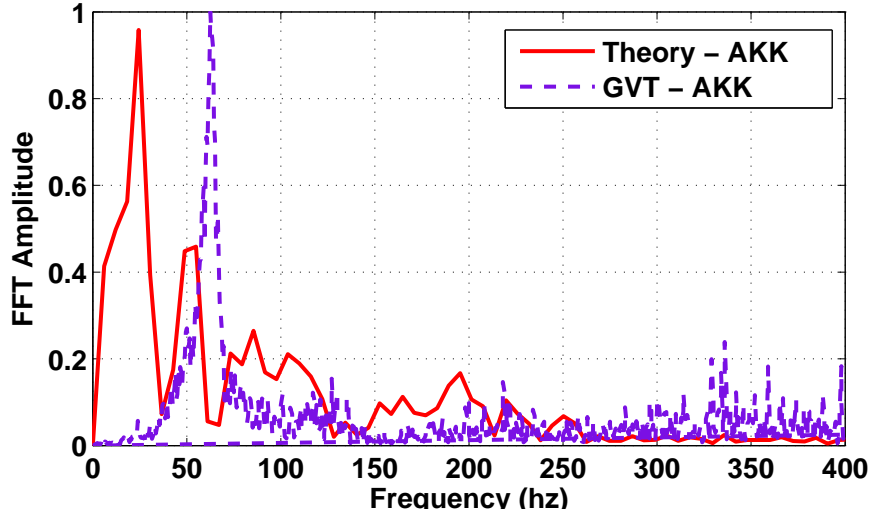


Figure 14: Impulse response of the AKK in model B and tunnel run 30.

5.2.3 Model C and tunnel run 31

The impulse response for model C and the GVT of the TPS coupon on the toroid simulator in tunnel run 31 are shown in Figure 15 for the outer Nextel and in Figure 16 for the AKK. There is generally good agreement for the first natural mode, and similar behavior is seen for the higher modes as well. Also, the AKK and Nextel layers have similar response throughout the entire frequency spectrum, which is in contrast to the results of the previous model. We attribute this to the fact that the AKK can deform around the toroid in response to forcing on the surface of the Nextel, thus allowing the layers to deflect in unison.

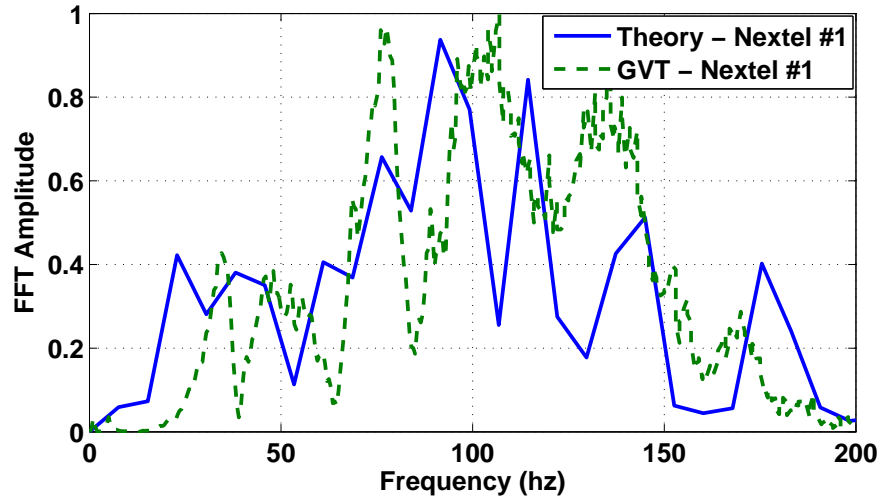


Figure 15: Impulse response of Nextel #1 in model C and tunnel run 31.

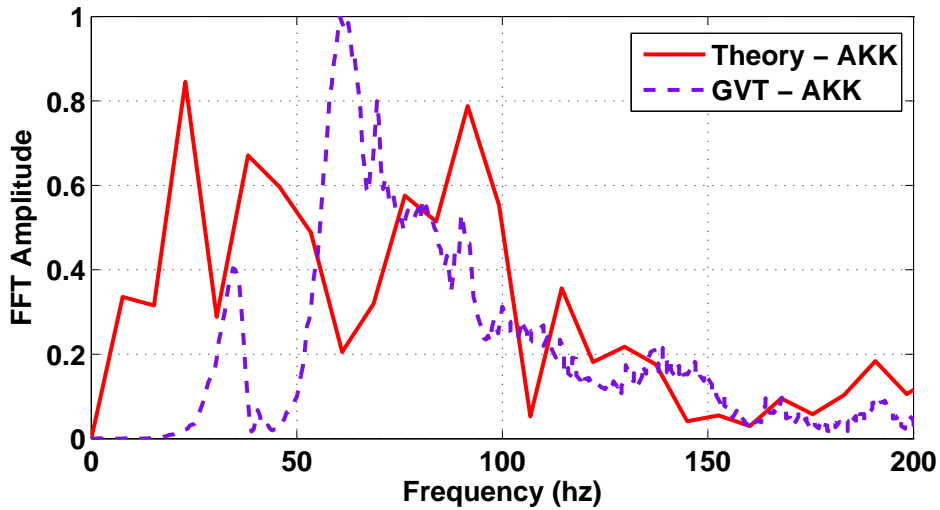


Figure 16: Impulse response of the AKK in model C and tunnel run 31.

5.2.4 Model D and tunnel runs 22 and 23

The impulse response for model D and the GVT of the *untensioned* simplified test article sample in tunnel run 22 are shown in Figure 17a. Since the bending stiffness of the sample is unknown, it was adjusted for the best possible fit to the experimental GVT result. The experimentally determined value of bending stiffness was then used in an impulse response free vibration calculation with added tension of 525 N/m, corresponding to the tension added to the experimental sample pre-run. A comparison between theory and experiment for this case is shown in Figure 17b. There is generally good agreement, though the frequencies of the experimental modes seem to be shifted

slightly from corresponding theoretical ones. There is currently no similar pre-run data available for tunnel run 23, but the samples are identical and should have similar properties.

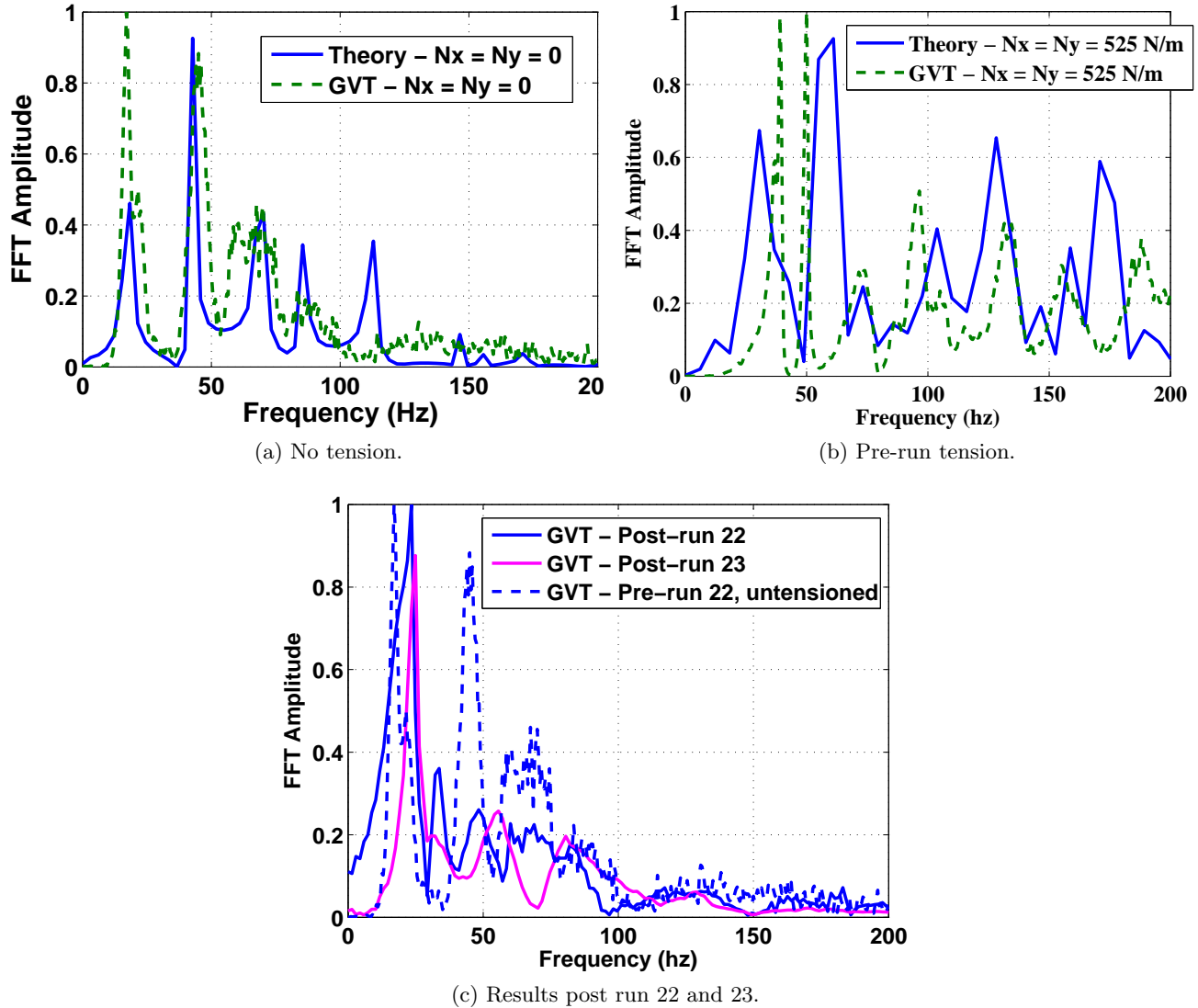


Figure 17: Impulse response of model D and tunnel runs 22 and 23.

GVTs of the samples were also conducted after the tunnel runs to assess the impact on material stiffness. As illustrated in Figure 17c, most of the pre-run applied tension has relaxed post-run since the measured post-run natural frequencies resemble those in the un-tensioned case. The frequencies are slightly higher in run 23, which indicates it had either higher initial tension or experienced less severe oscillations during the run. The latter has been verified by the accelerometer data and is discussed in subsection 5.3.4, but the former may also be true.

5.3 Theoretical and experimental aeroelastic response

In this section, the aeroelastic response of the various theoretical models are calculated and compared to the aeroelastic response of the corresponding samples in the tunnel. Detailed comparisons between theory and experiment for the TPS coupons will be made only for a Mach number and dynamic pressure corresponding to 5° angle of attack, since that is the case with available tunnel data. For the simplified test article sample in runs 22 and 23, data at both 2.5° and 5° angle of attack have been collected.

All deflections presented in this section will be normalized by the thickness of one layer of Nextel. Theoretical and experimental responses will be measured at the accelerometer location near the trailing edge of the sample, located at ξ (x/a), η (y/b) = 0.8, 0.5. For the calculations, 60 modes were used in the modal expansions for each of the TPS layers (10 modes in the stream-wise direction and 6 modes in the span-wise direction). This was found to be sufficient for a converged solution with respect to the maximum oscillation amplitude. The time required to compute 0.2 seconds of response is approximately 24 hours.

5.3.1 Model A and tunnel run 30 at 5° angle of attack

The theoretical and experimental deflection time histories of the outermost Nextel layer (referred to as Nextel #1) for model A and tunnel run 30 are given in Figure 18. The effect of the uni-directional Pyrogel foundation on the dynamics of the sample is demonstrated here, in that the theoretical deflection is shifted above $z = 0$, though some compression of the Pyrogel is evident. The experimental deflection experiences an even larger shift, though it is unclear if this is an artifact of the measurement apparatus. The amplitudes of the responses are of the same order but the experimental maximum amplitude is almost twice as large as that of the theory. It is also observed that the experimental response recorded by the photogrammetry has very little higher mode content. This is because the photogrammetry system has a sample rate of 500 Hz, which means the Nyquist cutoff frequency is 250 Hz. Any response in this frequency range will not be captured accurately and aliasing of higher modes may be occurring. This effect is demonstrated further in the frequency spectra of the responses in Figure 19. An FFT of the photogrammetry result indicates a single peak oscillation frequency at 110 Hz, but almost no response at 200 Hz. To see if this is actually the case, accelerometer data from the AKK in tunnel run 30 was used for comparison to determine if any part of the coupon exhibits higher mode behavior. Note that model B does not include the AKK, so the comparison is purely qualitative. The frequency spectrum of the AKK in Figure 19b does in fact show substantial higher mode content, so it is likely that the Nextel does as well. In fact, the theoretical Nextel and experimental AKK frequency spectra have similar characteristics, both showing rather noisy response near 250 Hz. This indicates that an FFT of the photogrammetry data is insufficient and will not be used for any further frequency analyses in this section. Instead, frequency response comparisons are only made using data from the accelerometers on the AKK.

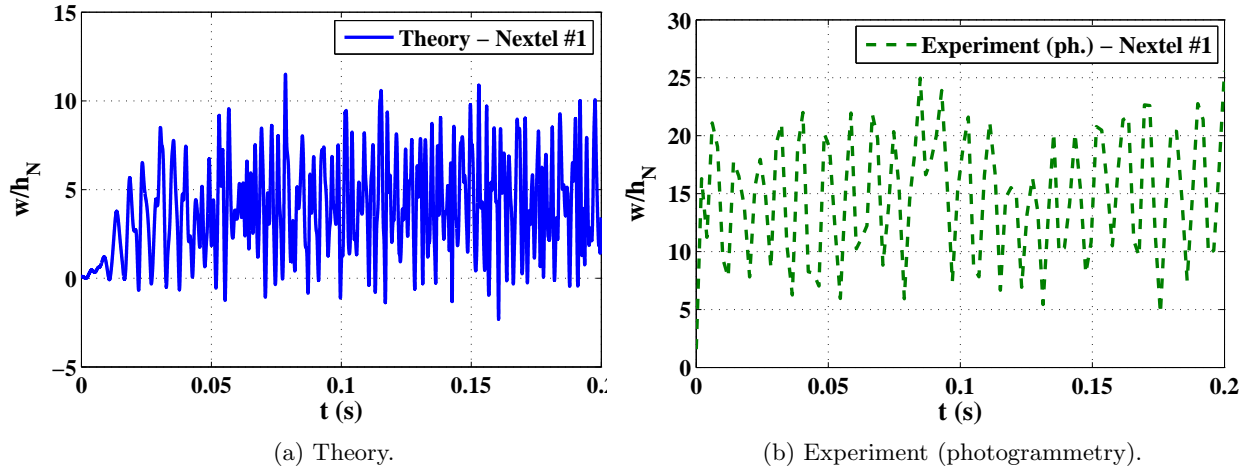


Figure 18: Time histories of the theoretical and experimental response of Nextel #1 in model A and tunnel run 30, at $\xi, \eta = 0.8, 0.5$.

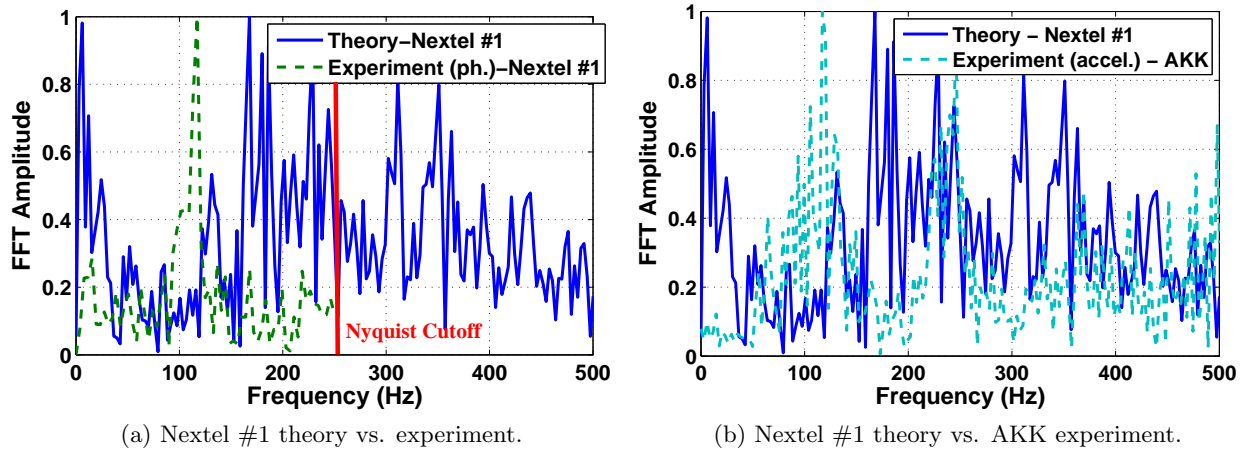


Figure 19: FFTs of the response time histories for model A and tunnel run 30, at $\xi, \eta = 0.8, 0.5$.

5.3.2 Model B and tunnel run 30 at 5° angle of attack

The theoretical deflection time histories of Nextel #1 and the AKK layer in model B are given in Figure 20. When sampled off a point-stitch, as in Figure 20, the outermost Nextel and AKK layers behave quite differently, with the Nextel amplitude significantly larger than that of the AKK. It is observed that the AKK never deflects below $z = 0$, while the Nextel does at a few points. This is because the foundation under the AKK has a spring stiffness orders of magnitude larger than that of the Pyrogel layer (which can be compressed by the Nextel). When sampled on a point-stitch, the layers move virtually in unison, indicating that the constraint method used is sufficient. Note that the initial positions of the layers are not included in theoretical time histories

given here. The separation between the outer Nextel and the AKK is equal to the thickness of the Pyrogel, which is approximately $16 \times h_N$.

We also draw comparisons between theory and experiment for this case. There is again a discrepancy between the oscillation amplitudes, though they are still of the same order. The larger experimental amplitude could be caused by many factors, including loosening of material at the trailing edge which is not considered in the theoretical models. With regard to frequency response, an FFT of the accelerometer data from the AKK during the test can be directly compared to the frequency response of the AKK in the theoretical model, which is shown in Figure 21. There is generally good agreement near 100 Hz, though the frequencies with maximum amplitude are shifted slightly. The theory also captures the experimental response in the AKK near 250 Hz. The experimental data has some frequency content well beyond 500 Hz, which is not captured by the theory. This content may be from other sources such as tunnel vibrations or pressure fluctuations. We also compare the theoretical frequency spectrum for Nextel #1 with the experimental result from the AKK accelerometer. This is shown in Figure 21b. The dominant frequency of the Nextel at 220 Hz is seen as a secondary peak in the spectrum of the AKK, which may indicate that the higher mode behavior of the Nextel is being transmitted through the Pyrogel to the AKK, or vice versa. High frequency measurements of the Nextel are needed to verify if this is actually occurring in the experimental configuration.

It may also be of interest to analyze the overall deflection behavior for both the theoretical model and the experimental sample. A three-dimensional colormap of the theoretical deflection at an arbitrary time is given in Figure 22a, and a photogrammetry overlay of run 30 at an arbitrary time are shown in Figure 22b. For both theory and experiment, the largest deflections are isolated in small patches towards the trailing edge of the sample. The behavior is chaotic in time and there is no symmetry in the span-wise direction. This behavior also demonstrates why it is necessary to retain many span-wise modes in the theoretical model.

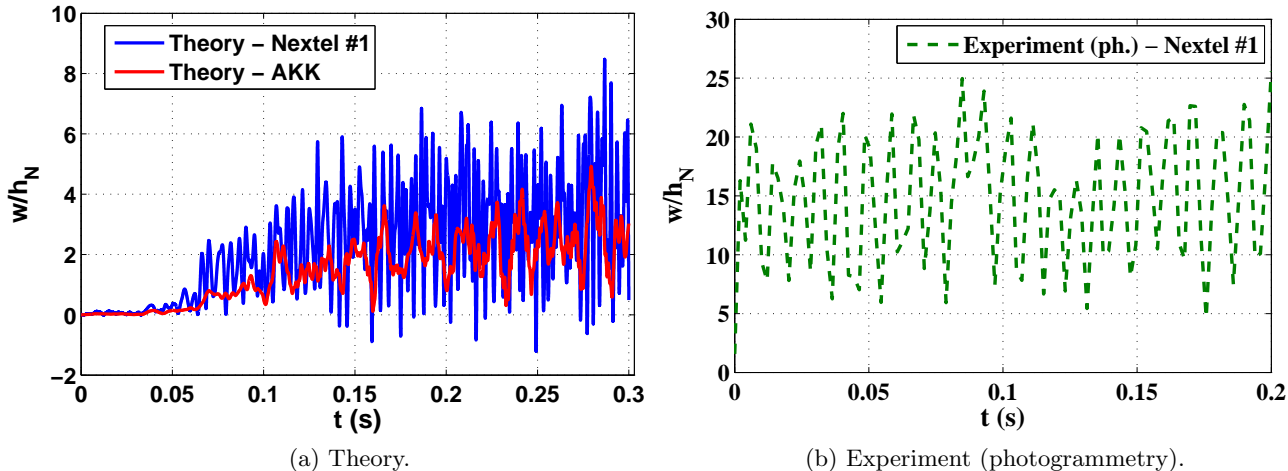


Figure 20: Time histories of the theoretical and experimental response of Nextel #1 and AKK in model B and Nextel #1 in tunnel run 30, at $\xi, \eta = 0.8, 0.5$.

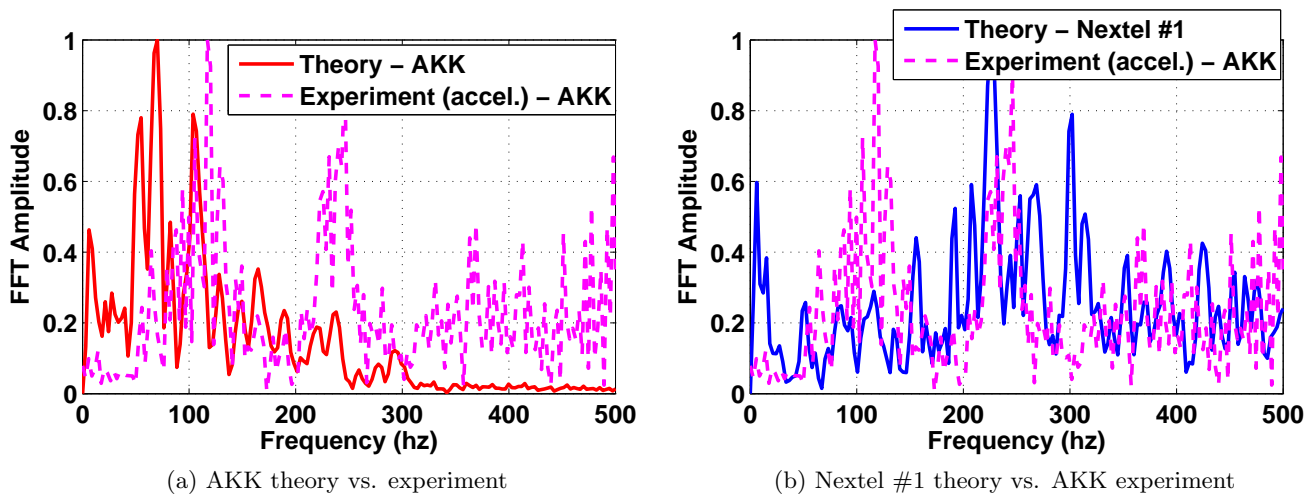


Figure 21: FTTs of the response time histories for model B and tunnel run 30, at $\xi, \eta = 0.8, 0.5$.

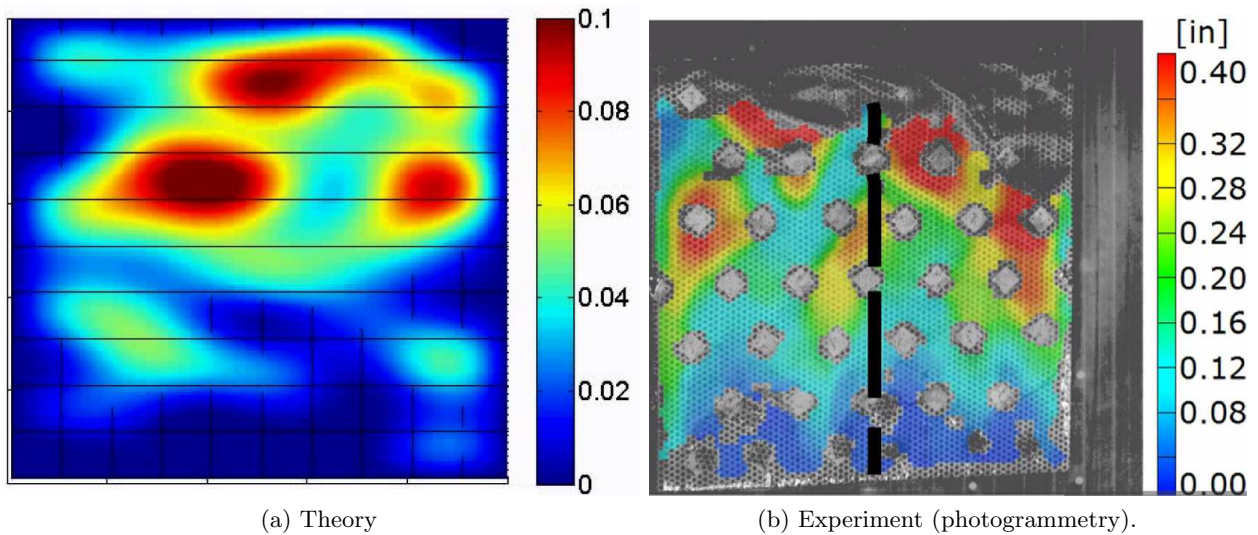


Figure 22: Deflection behavior of model B and tunnel run 30. Deflections are now in inches to match the photogrammetry format.

5.3.3 Model C and tunnel run 31 at 5° angle of attack

The theoretical deflection time histories for Nextel #1 and the AKK in model C are given in Figure 23a, while the experimental photogrammetry result is given in Figure 23b. In both theory and experiment, the sample oscillates about a position well below $z = 0$. This is because the imposed pressure differential deforms the material between the toroid foundation in the center and the edge of the sample. As in the previous two cases, there is still a discrepancy between theory and experiment in terms of the oscillation amplitude. However, we note that the maximum

amplitude in this model is larger than that of the previous model, which is in agreement with the experimental trend. Both theory and experiment clearly show that the toroid foundation results in larger amplitude oscillations near the trailing edge.

The frequency content of these results is given in Figure 24. In the case of the AKK, there is a single dominant frequency in the experimental data at 105 Hz, and a single dominant frequency in the theoretical result at 86 Hz. Some higher mode content in the AKK response is also seen, but the amplitude of this content with respect to the dominant frequency is low. The FFT of the theoretical Nextel response includes the same dominant frequency of 86 Hz along with a much more significant contribution from the higher modes. Again, as theorized for the previous model, the higher mode oscillations of the outer Nextel could be transmitted through the constraints and the Pyrogel to induce the higher mode oscillations in the AKK. This would be consistent with the significantly lower relative amplitude of the higher frequency content in the frequency spectrum of the AKK response.

The fact that there is a dominant “flutter” frequency in this case may be a consequence of the foundation upon which the sample rests. Ideally, the only difference between the present case and the previous cases is the type of foundation. The toroid foundation seems to limit the response of the sample to a certain narrow frequency range. This is expected, since the toroid acts as a divider between two material sections which are completely unsupported on their middle surfaces. This configuration approaches that of two plates on an open cavity, where one might expect more traditional panel flutter behavior.

The deflection shapes at arbitrary times for the theoretical model and the experimental result are given in Figure 25. A three-dimensional photogrammetry overlay was unavailable for run 31, but a two-dimensional overlay of the sample centerline was obtained. Therefore, a two-dimensional theoretical result has been provided in this case for proper comparison. In both theory and experiment, a relatively static hump in the middle of the sample is evident, which is due to the presence of the toroid. Deflections are isolated near the trailing edge, which is at the right hand side of both figures. Analysis of the experimental shape as a function of time indicated that the static deflections on either side of the toroid are present throughout the entire tunnel run. This indicates that a static pressure differential is present, which has been included in the theoretical model.

5.3.4 Model D and tunnel runs 22, 23 at 2.5°, 5° angle of attack

The theoretical and experimental results for the single-layer model and simplified test article are presented in this section. While there is currently no available photogrammetry data for deflection time histories, accelerometer response was recorded for both experimental runs and is given in Figure 26. The difference between the two runs is how the angle of attack was changed as a function of time. For run 22, the tunnel was initially set at 5° for 5 seconds and 2.5° for 3 seconds. For run 23, the tunnel was initially set at 2.5° for 3 seconds and 5° for 5 seconds. This procedure was implemented to see if the response trends were path dependent, i.e. if the sample exhibits hysteresis.

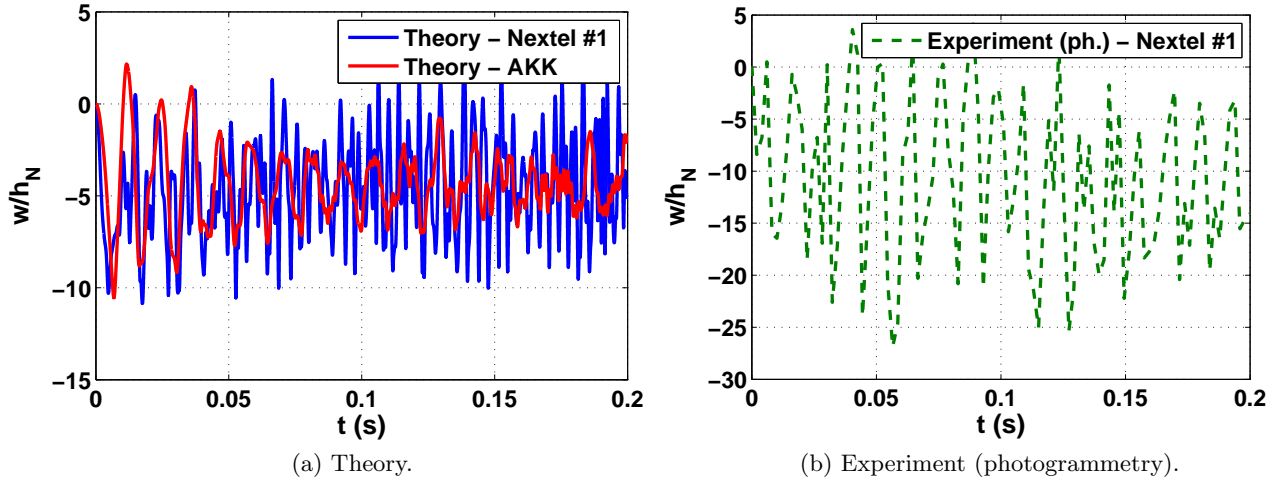


Figure 23: Time histories of the theoretical and experimental deflection response of Nextel #1 and AKK in model C and Nextel #1 in tunnel run 31, at $\xi, \eta = 0.8, 0.5$.

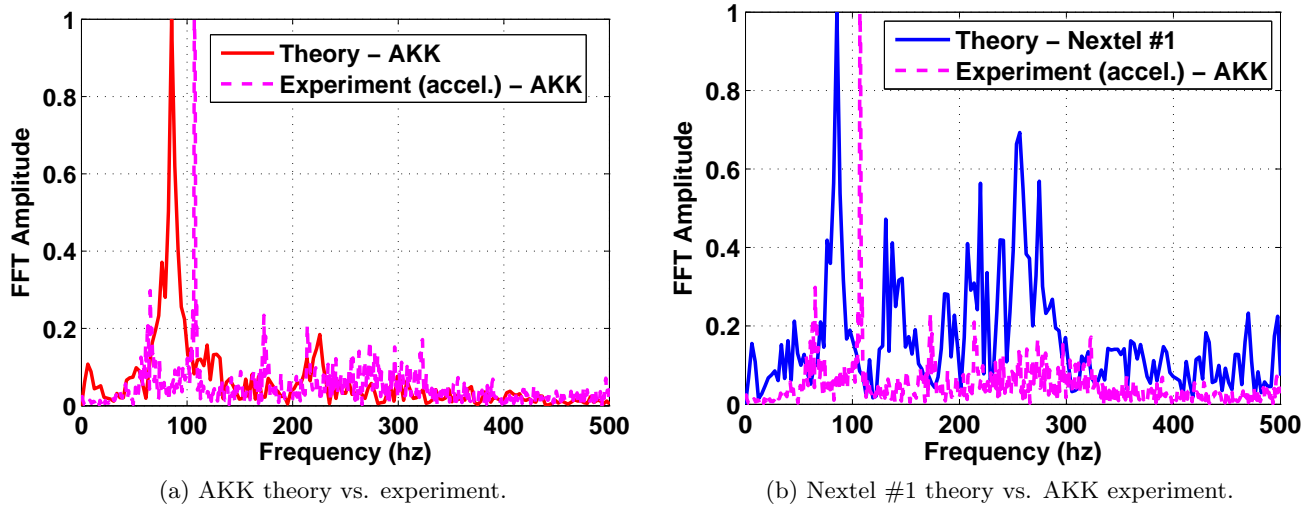
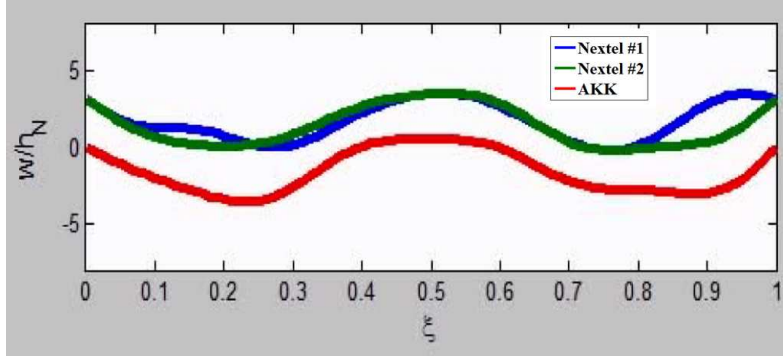
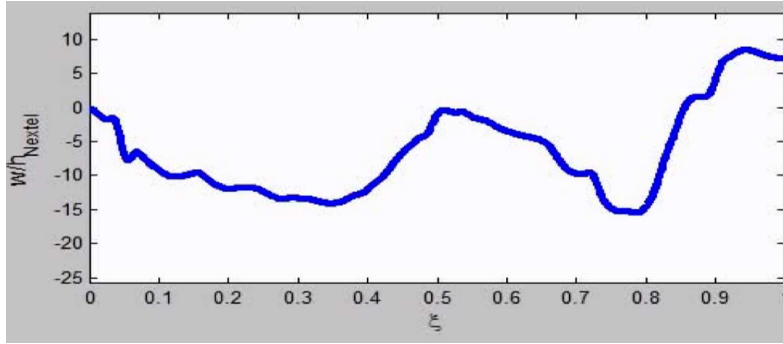


Figure 24: FFTs of the response time histories for model C and tunnel run 31, at $\xi, \eta = 0.8, 0.5$.

We observe several key features of these experimental results. First, based on maximum acceleration, the sample in run 22 was either more flexible than the sample in run 23 or was subject to greater dynamic pressure at all angles of attack. Theoretically, the run conditions at given angles should be the same, as well as the composition of the two samples and amount of initial tension. Several factors may be responsible for the discrepancy. Before the sample is injected into the flow, tunnel-cavity pressure fluctuations deform the sample, which relaxes some tension. It is possible that these fluctuations were more violent in run 22, thus reducing effective stiffness during the actual run. Indeed, the post run stiffness of the sample in run 23 decreased slightly less than the sample in run 22, which was noted earlier in Figure 17c. We also must consider imperfections in



(a) Theory - all layers.

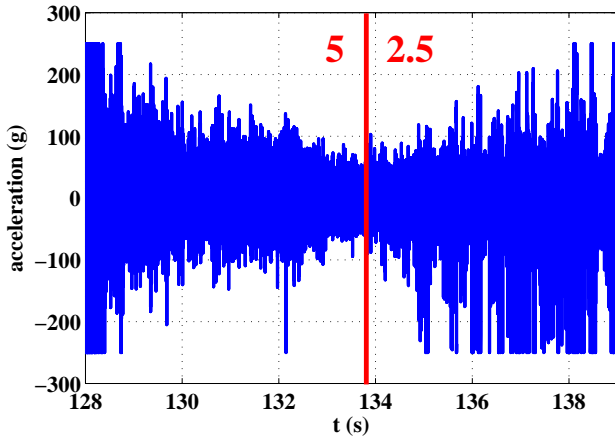


(b) Experiment - Nextel #1 (photogrammetry).

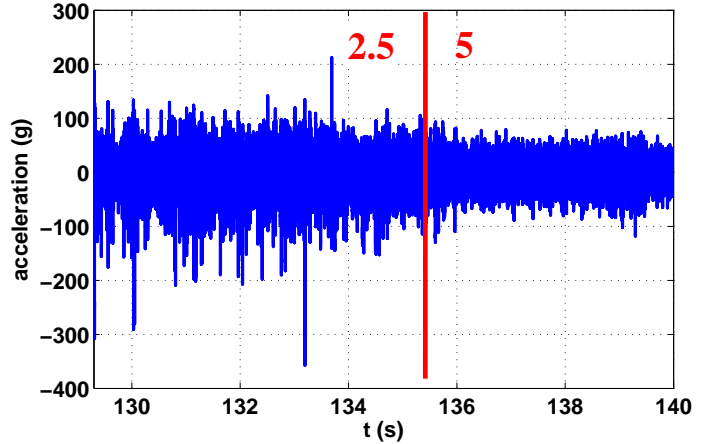
Figure 25: Theoretical and experimental deflection shapes on the sample centerline, at an arbitrary time.

the hand-made sample as well as slight differences in the initial boundary conditions (out-of-plane stiffness). Despite this discrepancy, the results from the two runs are consistent with each other in terms of overall trend in acceleration. The red vertical lines indicate when the angle of attack has changed from 5° to 2.5° in run 22 and from 2.5° to 5° in run 23. The sample at 2.5° has noticeably greater response in both runs. In run 22, it also appears that the flutter boundary has been crossed, since the acceleration decays initially and then grows as soon as the angle of attack changes to 2.5° . The reason for the greater response at 2.5° is not conclusively known. However, based on the deformation seen in high speed imaging of the runs, we believe the static pressure differential across the sample is likely greater at 5° . It is well known that a pressure differential across a panel has a stabilizing effect, since additional tension is induced from the static deformation. If the pressure differential is reduced from a large value, as is likely the case in run 22, the effective stiffness decreases and the oscillations grow. If the pressure differential is increased from a small value, as is likely the case in run 23, oscillations will tend to decay.

The frequency spectra corresponding to the acceleration time histories in Figure 26 are given in Figure 27. The FFT amplitudes at 5° are significantly lower than those at 2.5° , which is consistent with the time histories. There is a large amount of noise in both spectra, which may be due to fluid boundary layer fluctuations, or the nature of the nonlinear flutter behavior of the

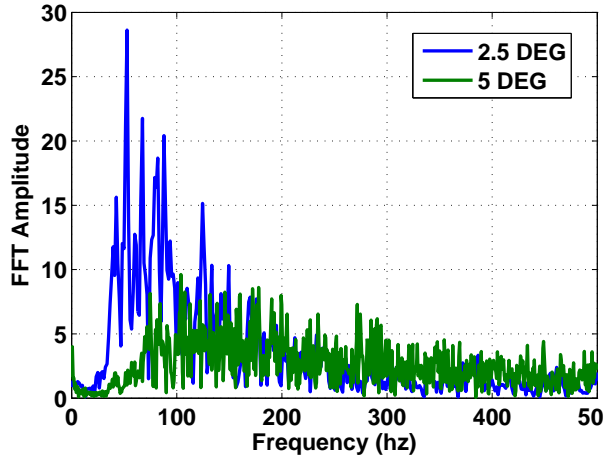


(a) Run 22.

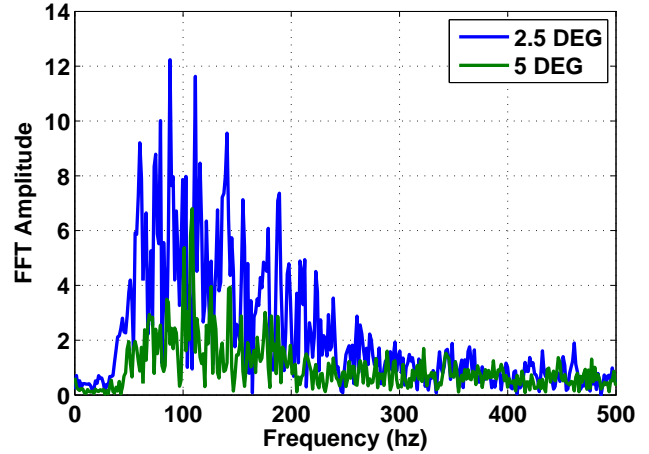


(b) Run 23.

Figure 26: Acceleration time histories of tunnel runs 22 and 23 at $\xi, \eta = 0.8, 0.5$. The red vertical line indicates a change in angle of attack.



(a) Run 22.



(b) Run 23.

Figure 27: FFTs of the acceleration response in tunnel runs 22 and 23 at $\xi, \eta = 0.8, 0.5$.

sample itself. However, peaks in the responses at 2.5° are observed at 52 Hz and 88 Hz for runs 22 and 23, respectively. The higher peak frequency and lower acceleration in run 23 should imply *lower deflection amplitudes*. To see if this is actually the case, we assume the following sinusoidal deflection response in time:

$$w(t) = \bar{w}e^{i\omega t} \quad (21)$$

where \bar{w} is the maximum amplitude of the deflection at the accelerometer location. Then the acceleration as a function of time is

$$\ddot{w}(t) = -\omega^2 \bar{w}e^{i\omega t} \quad (22)$$

and a sinusoidal approximation of the peak deflection amplitude is:

$$|\bar{w}| = \frac{\max(\ddot{w}(t))}{\omega^2} \quad (23)$$

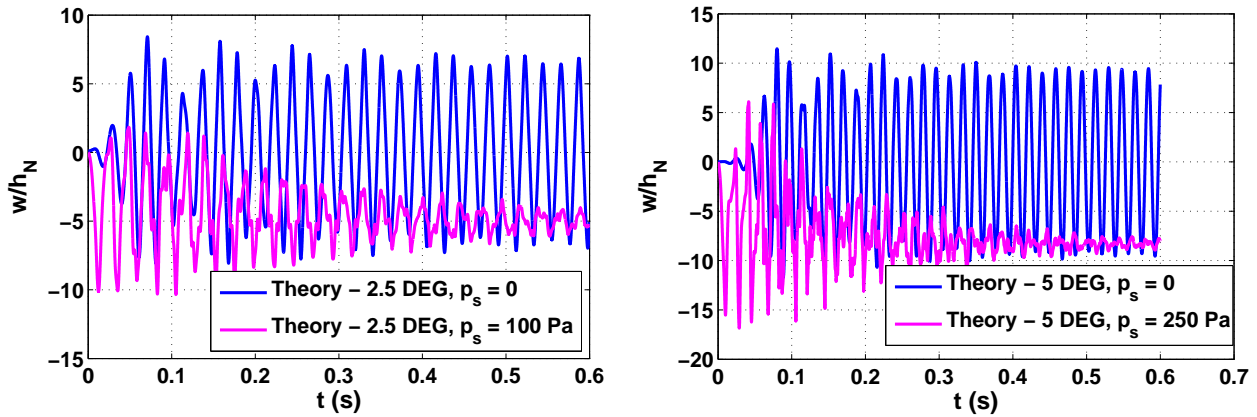
Using the maximum accelerations and peak frequencies in Figures 26 and 27, the approximate maximum deflections (at the accelerometer location) calculated using Eq. (23) is $55 \times h_N$ and $13 \times h_N$ for runs 22 and 23, respectively. High speed imaging of the runs suggest that these calculated amplitudes are likely too large, but this approximation does not consider the fact that energy is distributed among many frequencies. We can conclude that at 2.5° , the sample in run 22 had significantly larger deflection amplitudes than the sample in run 23.

Theoretical deflection time histories at both 2.5° and 5° are given in Figure 28. As discussed earlier, the Young's modulus needed to compute these results is unknown since three separate layers are stitched together to form a single layer. As a first approximation, the Young's modulus and thickness of the AKK were used, and the presence of the Nextel was included as added mass. No applied tension has been included here, which is more consistent with the state of the sample in run 22. The effect of static pressure differential p_s is to cause the oscillations to decay, with substantially less pressure needed at 2.5° than at 5° . No reliable experimental pressure differential data is currently available for an exact comparison. The theoretical and experimental frequency spectra are also given in Figure 29. Again, this comparison is made at 2.5° with no applied tension and no pressure differential included in the theory. Good agreement is seen for the peak oscillation frequency near 50 Hz, which suggests that the experimental sample at 2.5° has minimal static pressure differential and most tension has relaxed.

Unfortunately, the theoretical model cannot predict the peak frequency of 88 Hz seen in run 23. Assuming all of the 525 N/m of bi-axial tension has remained in the sample, theory predicts that oscillations decay at 2.5° . At higher dynamic pressures, the response frequencies increase slightly but do not approach 88 Hz. From these data, we hypothesize that flutter (LCO) is not the main cause of the oscillations in run 23. Another excitation source such as turbulent boundary layer fluctuations may be responsible for the accelerometer response in this case. This is consistent with the much lower approximate amplitudes calculated for run 23 using Eq.(23). Based on these data, it is also difficult to draw a conclusion regarding the angle of attack hysteresis, since the oscillation frequencies of the two runs are not the same.

Since the complexity and computation time of the single-layer model is relatively low, some additional parameter studies have been included in this section that were not included for the previous models. The effect of applied tension and static pressure differential on the theoretical oscillation amplitudes over all angles of attack is shown in Figure 30. For additional physical insight into the previously discussed foundations, the effect of adding a uni-directional Pyrogel foundation to the single layer model is also included.

Adding tension and a pressure differential to the system increases the flutter boundary, meaning that a higher dynamic pressure (and thus larger angle of attack) is needed for flutter onset. Higher tension also seems to reduce the maximum oscillation amplitude at high angle of attack, while the higher pressure differential has less of an effect. This is demonstrated most clearly at 7.5° , where the cases with added pressure have nearly the same amplitude as the single layer alone.



(a) Effect of pressure differential at 2.5° angle of attack. (b) Effect of pressure differential at 5° angle of attack.

Figure 28: Effect of pressure differential on the theoretical LCO behavior of model D at $\xi, \eta = 0.8, 0.5$, with no applied tension.

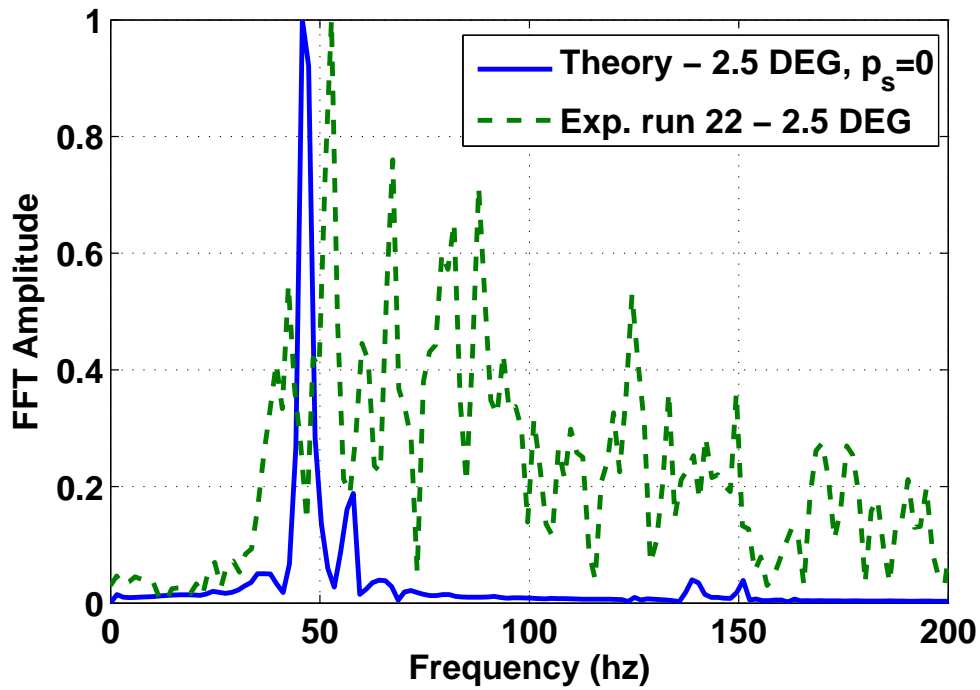


Figure 29: FFTs of the deflection time histories for model D and tunnel run 22, at $\xi, \eta = 0.8, 0.5$.

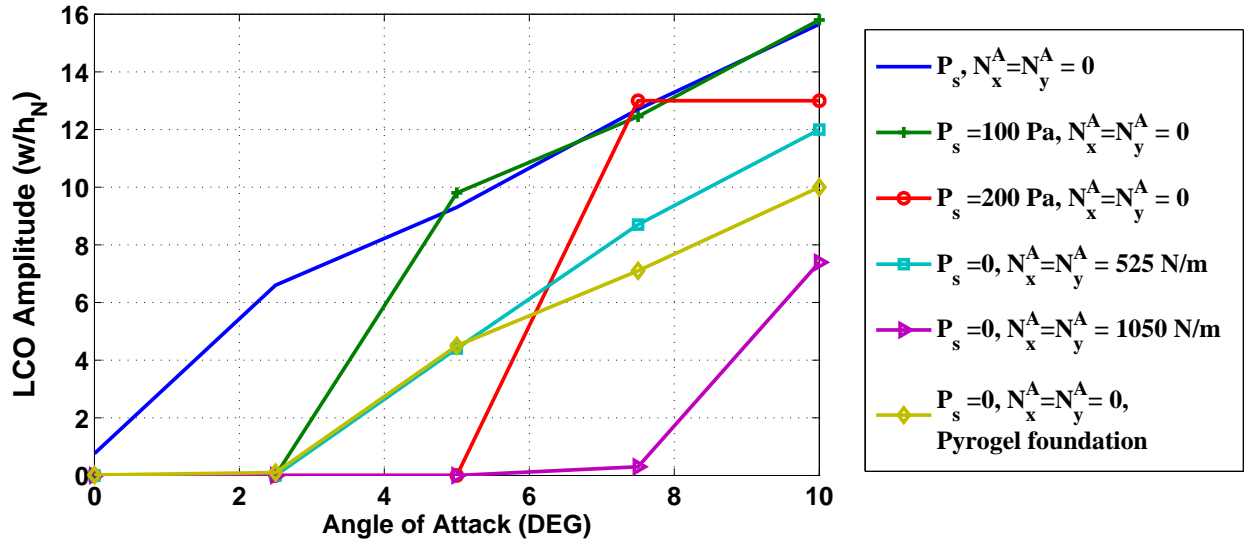


Figure 30: Effect of tension, static pressure, and a uni-directional Pyrogel foundation on model D, at all angles of attack in the tunnel.

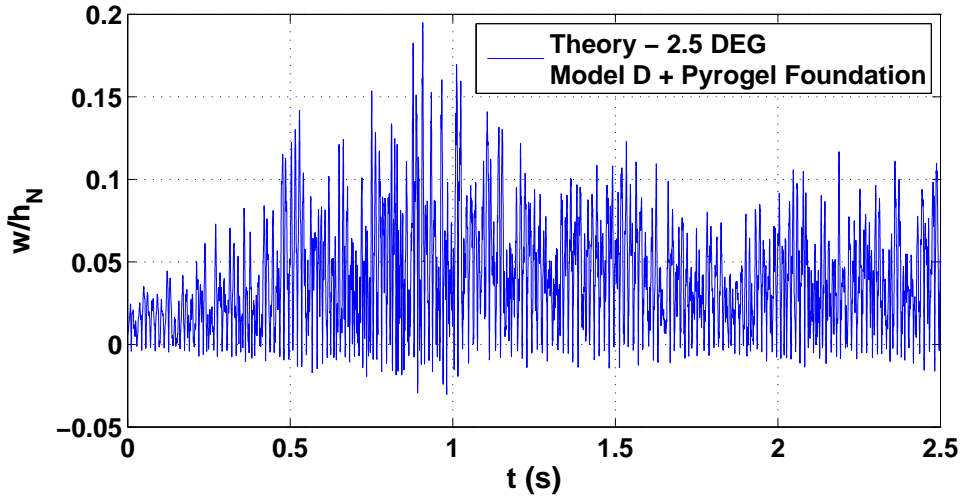


Figure 31: Chaotic oscillations of the simplified test article on a uni-directional Pyrogel foundation, at 2.5° angle of attack.

If the open cavity in model D is replaced with a uni-directional Pyrogel foundation, the oscillation amplitudes are reduced considerably from that of the single layer on an open cavity, though the amplitudes are comparable to those with 525 N/m tension. The most notable result here can only be seen by examining the time histories at low angle of attack. Though it looks like the amplitudes are zero for the Pyrogel foundation case at 0° and 2.5° , there are actually chaotic oscillations on the order of $1/10^{\text{th}}$ the thickness that do not decay with time. This is in contrast to the cases with pressure differential and tension, where the oscillations do decay with time for the same angles of attack. Therefore, the effect of the foundation is to not only reduce the maximum oscillation amplitude but also induce instability *earlier* than most other test cases. The chaotic

behavior of this case is illustrated in Figure 31. In addition, we observe that the amplitude at 5° is significantly greater with the foundation than with a pressure differential of 200 Pa. This also demonstrates how the foundation is not always a stabilizing factor, especially when compared to a pressure differential.

6 Preliminary analysis of in-flight stability

To accurately assess stability of the TPS on the HIAD vehicle, it is necessary to match the parameters in the theoretical aeroelastic models to those in flight. These parameters include the structural geometry, boundary conditions, Mach number, dynamic pressure, and static pressure differential. While the coupon is a square panel, the TPS on the HIAD is a truncated conical shell, so a new structural model is needed for a complete aeroelastic analysis of the in-flight configuration. However, suppose we consider a square section of the TPS shell on the HIAD which has the same dimensions as the coupon. If the cone angle is large enough, a section near the shell trailing edge will be relatively flat, and a qualitative comparison can be made with the aeroelastic models in this paper. Additionally, the distance between the toroid edge and the trailing edge in the coupon tests is approximately equal to the toroid separation distance on the HIAD. Since the TPS shell rests directly on the toroids, a square section in the correct position “feels” unidirectional stiffness at locations in the flow direction where the restrained edges exist in the coupon tests. Due to this local geometric similarity, it may be of interest to calculate an aeroelastic solution using the toroid-foundation coupon model with the in-flight local flow parameters.

Here, we consider CFD simulations [10] of the 70° half-cone angle, 3m diameter HIAD during the peak heating condition of a proposed re-entry trajectory. The local Mach number and dynamic pressure on the TPS surface, for 0° and 15° angle of attack, are given in Figure 32. The peak heating condition does not necessarily correspond to the highest Mach numbers and dynamic pressures seen in the trajectory, but these are the data currently available. At 0° angle of attack, most of the TPS surface is subsonic/transonic, so current aeroelastic models cannot be applied. However, at 15° angle of attack, the upper trailing edge of the cone is supersonic (with a Mach number high enough such that piston theory can be applied). This will be the region of interest for the following coupon analysis.

A theoretical aeroelastic solution was computed using the three-layer toroid foundation model with $M=2$, $q=1400$ Pa, and $p_s=250$ Pa. The static pressure differential (p_s) is unknown but was assumed to be the same as that of the previous tunnel simulations. This is likely smaller than what would be observed during re-entry, but any additional pressure differential should have a stabilizing effect. Also, both the Mach number and dynamic pressure are significantly lower than in the 8’ HTT at all angles of attack. The theoretical deflection time history for the outermost Nextel layer is given in Figure 33. During the first 0.1s of simulation, only the static pressure differential acts on the sample, resulting in initial deformation of the TPS between the toroid and the trailing edge. At $t=0.1s$, the sample is perturbed and the aerodynamic forces are applied. The oscillations resulting from this perturbation decay with time, unlike the deflection time history of the TPS coupon in the 8’ HTT (see Figure 23a).

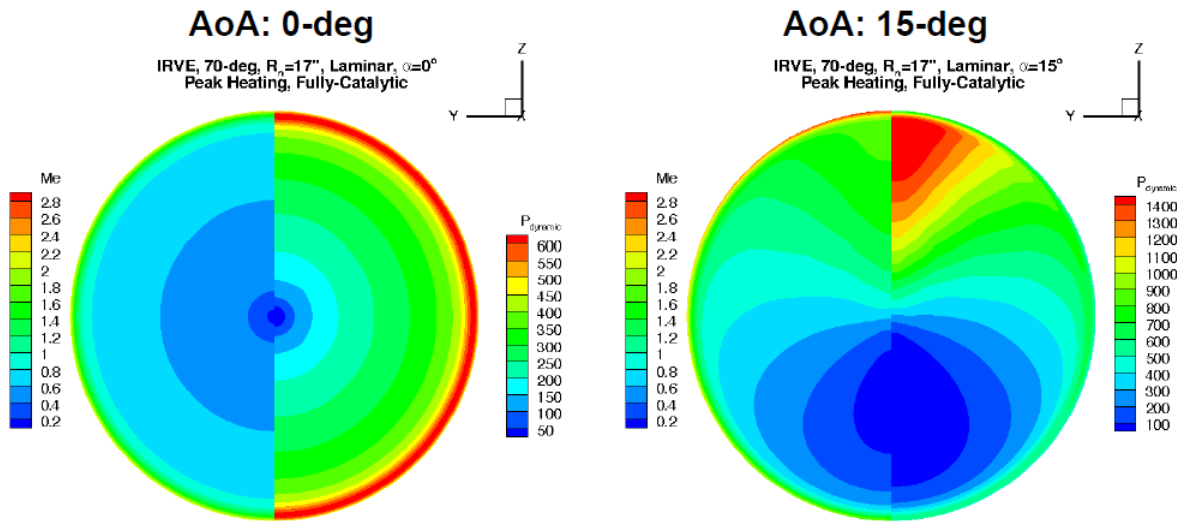


Figure 32: Local flow parameters at the peak heating condition of a proposed re-entry trajectory. Note: the left half of each plot shows the local Mach number, and the right half shows local dynamic pressure.

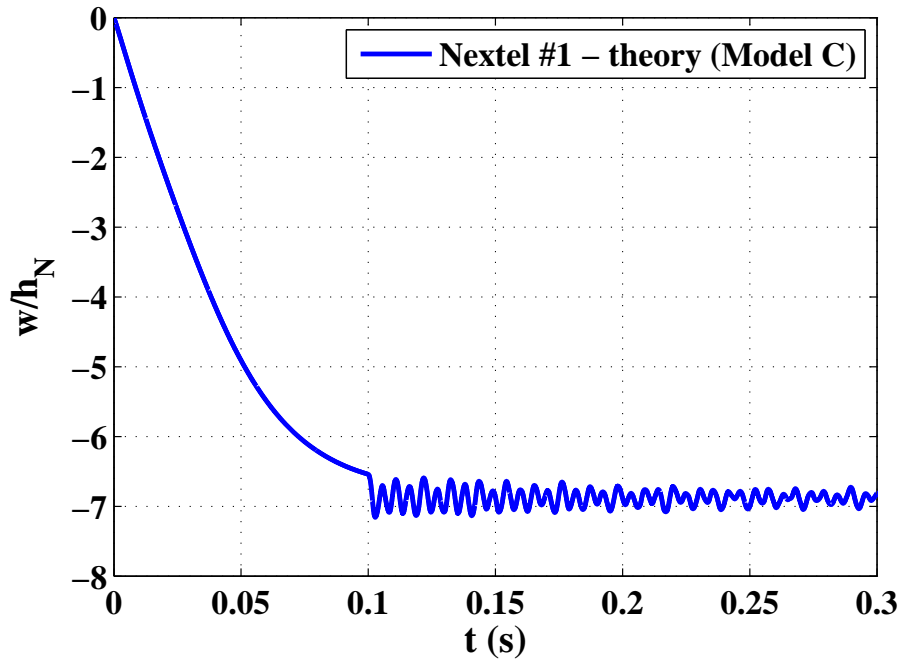


Figure 33: Theoretical deflection time history of Nextel #1 in Model C, with trajectory (peak heating) flow parameters, at $\xi, \eta = 0.8, 0.5$.

These results suggest that a hypothetical TPS “coupon” near the trailing edge of the 3m HIAD (at 15° angle of attack, during peak heating) is unlikely to flutter. Local flow parameters are needed before and after the peak heating condition to verify that this is the case for the entire trajectory. While the TPS coupon is stable here, it is still unknown if the TPS shell will exhibit similar stability, since the natural modes and frequencies are different. An aeroelastic evaluation incorporating the HIAD vehicle geometry is still necessary to verify that flutter will not occur in-flight.

7 Concluding Remarks

A theoretical and experimental aeroelastic analysis of the generation 1 HIAD TPS coupon, consisting of Nextel 440-BF20, Pyrogel 2250, and AKK, has been presented in this paper. Several experimental configurations were tested in the NASA 8’ High Temperature Tunnel and corresponding theoretical models were developed. In both theory and experiment, aeroelastic flutter manifesting as limit cycle oscillations were observed for the TPS coupon resting on both a flat and toroid foundation. The experimental deflection amplitudes were generally twice as large as those predicted by theory, which may indicate degradation or material loosening during the wind tunnel tests. Since the maximum amplitudes were calculated for the theoretical model with only two contained layers of Nextel, it is likely that stitch detachment between the Nextels and AKK in the experiments is also a contributing factor to the larger observed amplitudes. Fourier transforms of the theoretical deflection and experimental acceleration time histories also provided additional insight into the dynamics of the system. The higher mode response of the AKK layer was similar to that of the theoretical Nextel response, indicating that oscillations of the Nextel may be transmitted through the Pyrogel to excite the AKK. There was also good agreement between theoretical and experimental peak oscillation frequencies for the toroid foundation case - model C and tunnel run 31. It was determined that the toroid has the effect of reducing chaos, since the frequency response was predominantly at a single peak frequency. Effectively, the toroid acts as a spacial divider between two samples resting on two separate open cavities.

In addition to the TPS coupon, a simplified test article/open cavity configuration was developed to simplify the aeroelastic modeling and limit the number of unknowns in comparing theory and experiment. While the structural model is significantly simpler in theory, it turns out that this reduction actually adds some complexity to the on-air tunnel runs. The lack of foundation underneath the sample allows downward static deformation, due to the static pressure differential which is also function of the angle of attack. It was observed that the open cavity permitted higher static pressure differentials at higher angles of attack, resulting in the decay of oscillations despite *increasing dynamic pressure*. In contrast, amplitude measurements from previously tested TPS coupons on flat foundations indicated that oscillation amplitude grows with angle of attack, presumably because the foundation prevents static deformation induced tension. In addition, the presence of only one layer in these experimental tests (as opposed to four in the TPS coupon), may result in greater sensitivity to applied tension. This is demonstrated by the difference in acceleration response between the two supposedly identical experimental tunnel runs (22 and 23). We hypothesize that slight differences in initial tension, caused by variations in the tensioning system

or pre-run tunnel pressure fluctuations, were likely responsible for this difference. The open-cavity experiments suggest that the stability of the in-flight article will be impacted by the static pressure differential and applied tension, as well as the flow dynamic pressure.

The aeroelastic stability of the in-flight configuration was also considered by calculating the deflection response of the three-layer toroid foundation model using local flow parameters from a proposed re-entry trajectory. While the overall geometry of the HIAD vehicle is considerably different from the TPS coupon, local structural similarities in the flow direction allowed a qualitative assessment of the in-flight behavior. In this case, it was observed that oscillations of the coupon decay with time, indicating that the flutter condition had not been achieved. Since this calculation does not take into account the conical shape of the TPS shell, a final conclusion cannot yet be made regarding in-flight stability.

Appendix

The equations of motion for all four models are given in this section. The equations have been vectorized in a manner such that the systems of ODEs can be solved without loops involving the modal coordinates. These types of iteration statements within ODE solvers are computationally costly, especially for interpreted programming languages. Loops may be used in the construction of some of the higher order tensor coefficients that are constant with respect to time, and can thus be computed outside of the ODE solving routine. This procedure results in optimum computational performance with respect to the MATLAB ODE45 solver.

Model A

The aeroelastic equations of motion for model A are:

$$\begin{aligned}
 M^{N1} \ddot{\vec{a}} + Z^{N1} \dot{\vec{a}} + [B^{N1} + A^{N1}] \vec{a} + I^{N1} \{ \vec{a} - \vec{b} \} + S^{N1} + F^{N1} &= 0 \\
 M^{N2} \ddot{\vec{b}} + Z^{N2} \dot{\vec{b}} + B^{N2} \vec{b} + I^{N2} \{ \vec{b} - \vec{a} \} + S^{N2} + F^{N2} &= 0
 \end{aligned}
 \tag{A1}$$

where \vec{a} and \vec{b} are the modal coordinate vectors of the two separate Nextel layers (each term in the equations is an N vector). The coefficient matrices in the above equations involve integrals of the mode shape functions. The simply-supported mode shape function for a given mode number n is an $r_x \times r_y$ matrix defined as:

$$\phi_n = \phi_{nm} = \sin(n\pi\xi) \otimes \sin(m\pi\eta)
 \tag{A2}$$

where $\xi = x/a$, $\eta = y/b$, and r_x and r_y are the number of discrete points in the numerical discretization of the mode shape, in the x and y directions, respectively. The symbol \otimes is the vector outer product. Note that the n^{th} stream-wise mode and the m^{th} span-wise mode are specified by a single modal index n , and a numerical algorithm generates the correct modal indexing for both directions. While ϕ_n is a matrix, the data structure Φ is a third order tensor comprised of modeshapes $1 \dots N$, where N is the total number of modes. Thus Φ has dimensions $r_x \times r_y \times N$. The square of the mode shape tensor is computed using the element-wise Schur product in three dimensions, known by the symbol \circ .

The diagonal mass matrices are:

$$\begin{aligned}
 M_{nn}^{N1} &= m^{N1} \int_0^1 \int_0^1 \Phi \circ \Phi d\xi d\eta \\
 M_{nn}^{N2} &= m^{N2} \int_0^1 \int_0^1 \Phi \circ \Phi d\xi d\eta
 \end{aligned}
 \tag{A3}$$

The diagonal coefficient matrices involving the bending and applied tension terms are:

$$B_{nn}^{N1} = D^{N1} \int_0^1 \int_0^1 \left\{ \frac{1}{a^4} \frac{\partial^2 \Phi}{\partial \xi^2} \circ \frac{\partial^2 \Phi}{\partial \xi^2} + \frac{1}{b^4} \frac{\partial^2 \Phi}{\partial \eta^2} \circ \frac{\partial^2 \Phi}{\partial \eta^2} + \frac{2\nu^{N1}}{(ab)^2} \frac{\partial^2 \Phi}{\partial \xi^2} \circ \frac{\partial^2 \Phi}{\partial \eta^2} + \frac{2(1-\nu^{N1})}{(ab)^2} \frac{\partial^2 \Phi}{\partial \xi \partial \eta} \circ \frac{\partial^2 \Phi}{\partial \xi \partial \eta} \right\} d\xi d\eta$$

$$+ \frac{N_x^{A-N1}}{a^2} \int_0^1 \int_0^1 \frac{\partial \Phi}{\partial \xi} \circ \frac{\partial \Phi}{\partial \xi} d\xi d\eta + \frac{N_y^{A-N1}}{b^2} \int_0^1 \int_0^1 \frac{\partial \Phi}{\partial \eta} \circ \frac{\partial \Phi}{\partial \eta} d\xi d\eta \quad (\text{A4})$$

$$B_{nn}^{N2} = D^{N2} \int_0^1 \int_0^1 \left\{ \frac{1}{a^4} \frac{\partial^2 \Phi}{\partial \xi^2} \circ \frac{\partial^2 \Phi}{\partial \xi^2} + \frac{1}{b^4} \frac{\partial^2 \Phi}{\partial \eta^2} \circ \frac{\partial^2 \Phi}{\partial \eta^2} + \frac{2\nu^{N2}}{(ab)^2} \frac{\partial^2 \Phi}{\partial \xi^2} \circ \frac{\partial^2 \Phi}{\partial \eta^2} + \frac{2(1-\nu^{N2})}{(ab)^2} \frac{\partial^2 \Phi}{\partial \xi \partial \eta} \circ \frac{\partial^2 \Phi}{\partial \xi \partial \eta} \right\} d\xi d\eta$$

$$+ \frac{N_x^{A-N2}}{a^2} \int_0^1 \int_0^1 \frac{\partial \Phi}{\partial \xi} \circ \frac{\partial \Phi}{\partial \xi} d\xi d\eta + \frac{N_y^{A-N2}}{b^2} \int_0^1 \int_0^1 \frac{\partial \Phi}{\partial \eta} \circ \frac{\partial \Phi}{\partial \eta} d\xi d\eta$$

The coefficient matrix for the spring stitching (for point-wise stitching only) is:

$$I_{ni}^{N1} = I_{ni}^{N2} = k^{St} \sum_j \phi_n(\xi = \xi_j, \eta = \eta_j) \phi_i(\xi = \xi_j, \eta = \eta_j) \quad (\text{A5})$$

where the summation over index j refers to the individual point stitches in the system. Note that I_{ni}^{N1} would not be equivalent to I_{ni}^{N2} if different modal functions were used for the two Nextel layers. Coefficient matrix for the aerodynamic stiffness is:

$$A_{ni}^{N1} = \frac{2q}{Ma} \int_0^1 \int_0^1 \frac{\partial \phi_i}{\partial \xi} \circ \phi_n d\xi d\eta \quad (\text{A6})$$

The coefficient matrix for aerodynamic damping is:

$$Z_{nn}^{N1} = Z_{nn}^{N2} = \frac{2q}{MU_\infty} \int_0^1 \int_0^1 \Phi \circ \Phi d\xi d\eta = \rho_\infty a_\infty \int_0^1 \int_0^1 \Phi \circ \Phi d\xi d\eta \quad (\text{A7})$$

The Pyrogel foundation vector is a nonlinear function of the modal coordinate and is given by:

$$F_n^{N1} = k^{Pyr} \int_0^1 \int_0^1 H[-\Phi \bar{\times}_3 \bar{a}] \circ \left\{ \Lambda \bar{\times}_4 \bar{a} \right\} d\xi d\eta \quad (\text{A8})$$

$$F_n^{N2} = k^{Pyr} \int_0^1 \int_0^1 H[-\Phi \bar{\times}_3 \bar{b}] \circ \left\{ \Lambda \bar{\times}_4 \bar{b} \right\} d\xi d\eta$$

where $\bar{\times}_n$ is defined by Bader and Kolda [19] as the product of a tensor and a vector in the tensor's n th dimension. The two quantities on either side of the Shur product operator inside the integrals in Eq. (A8) will have different dimensions unless they are reshaped accordingly. Λ is a 4th order tensor defined by:

$$\Lambda_{ijkl} = \Phi_{ijk} \Phi_{ijl} \quad (\text{A9})$$

Here the repeated indices do not indicate summation. Note that Eq. (A8) requires one numerical integration at every time step in the ODE solver.

The stretching energy vector is a nonlinear function of the modal coordinate and is given by:

$$S_n^{N1} = \text{sum} \left\{ \Gamma_{nijk}^{N1} \mid k = 1, \dots, N; j = 1, \dots, N; i = 1, \dots, N \right\} \quad \text{for } n = 1, \dots, N$$

$$S_n^{N2} = \text{sum} \left\{ \Gamma_{nijk}^{N2} \mid k = 1, \dots, N; j = 1, \dots, N; i = 1, \dots, N \right\} \quad \text{for } n = 1, \dots, N \quad (\text{A10})$$

with

$$\begin{aligned}\Gamma^{N1} &= \left((\vec{a} \otimes \vec{a}) \otimes (\vec{1} \otimes \vec{a}) \right) \circ \Omega \\ \Gamma^{N2} &= \left((\vec{b} \otimes \vec{b}) \otimes (\vec{1} \otimes \vec{b}) \right) \circ \Omega\end{aligned}\tag{A11}$$

where $\vec{1}$ is a vector of ones the same length as the modal coordinate vector. The notation in Eq. (A10) is discussed in detail by Bader and Kolda [19]. The sum operation indicates summation of the specified tensorial dimensions and subsequent reduction in tensor order, or ‘‘tensorial collapsing.’’ The dimensions to be collapsed here are the fourth, third, and second dimensions, indicated by i , j and k , respectively. Note that the Schur product now acts in four dimensions. The fourth order tensor coefficient Ω for the n th mode is given by:

$$\Omega_{n i j s} = \sum_k \frac{1}{2Eh} \left(\frac{a}{b} \right)^4 R_k C_k^2 \{ \alpha_{nik} \alpha_{j s k} + \alpha_{ink} \alpha_{j s k} + \alpha_{j i k} \alpha_{n s k} + \alpha_{s i k} \alpha_{j n k} \}\tag{A11}$$

where E and h refer to the given plate layer (Nextel only in this case) and

$$\begin{aligned}R_k &= \int_0^1 \int_0^1 \left\{ \frac{1}{a^4} \frac{\partial^2 \Phi}{\partial \xi^2} \circ \frac{\partial^2 \Phi}{\partial \xi^2} + \frac{1}{b^4} \frac{\partial^2 \Phi}{\partial \eta^2} \circ \frac{\partial^2 \Phi}{\partial \eta^2} - \frac{2\nu}{(ab)^2} \frac{\partial^2 \Phi}{\partial \xi^2} \circ \frac{\partial^2 \Phi}{\partial \eta^2} + \frac{2(1+\nu)}{(ab)^2} \frac{\partial^2 \Phi}{\partial \xi \partial \eta} \circ \frac{\partial^2 \Phi}{\partial \xi \partial \eta} \right\} d\xi d\eta \\ C_k &= \frac{Eh}{\int_0^1 \int_0^1 \left\{ \frac{\partial^4 \Phi}{\partial \xi^4} \circ \Phi + \left(\frac{a}{b} \right)^4 \frac{\partial^4 \Phi}{\partial \eta^4} \circ \Phi + 2 \left(\frac{a}{b} \right)^2 \frac{\partial^2 \Phi}{\partial \xi^2} \circ \frac{\partial^2 \Phi}{\partial \eta^2} \right\} d\xi d\eta} \\ \alpha_{nik} &= \beta_{nik} - \gamma_{nik}\end{aligned}\tag{A12}$$

$$\beta_{nik} = \int_0^1 \int_0^1 \frac{\partial^2 \phi_n}{\partial \xi \partial \eta} \circ \frac{\partial^2 \phi_i}{\partial \xi \partial \eta} \circ \phi_k d\xi d\eta$$

$$\gamma_{nik} = \int_0^1 \int_0^1 \frac{\partial^2 \phi_n}{\partial \xi^2} \circ \frac{\partial^2 \phi_i}{\partial \eta^2} \circ \phi_k d\xi d\eta$$

Model B

The aeroelastic equations of motion for model B are:

$$\begin{aligned}M^{N1} \ddot{\vec{a}} + Z^{N1} \dot{\vec{a}} + [B^{N1} + A^{N1}] \vec{a} + I^{N1} \left\{ \vec{a} - \vec{b} \right\} + S^{N1} + F^{N1} &= 0 \\ M^{N2} \ddot{\vec{b}} + Z^{N2} \dot{\vec{b}} + B^{N2} \vec{b} + I^{N2} \left\{ \vec{b} - \vec{a} \right\} + I^{N2} \left\{ \vec{b} - \vec{c} \right\} + G^{N2} \left\{ \vec{b} - \vec{c} \right\} + S^{N2} + F^{N2} &= 0 \\ M^K \ddot{\vec{c}} + Z^K \dot{\vec{c}} + B^K \vec{c} + I^K \left\{ \vec{c} - \vec{b} \right\} + G^K \left\{ \vec{c} - \vec{b} \right\} + S^K + F^K &= 0\end{aligned}\tag{A13}$$

The terms M^{N1} , M^{N2} , Z^{N1} , Z^{N2} , A^{N1} , B^{N1} , B^{N2} , I^{N1} , I^{N2} , S^{N1} , S^{N2} , F^{N1} , and F^{N2} are the same as previous, and M^K , Z^K , B^K , I^K and S^K are the same except with substitution of the AKK material properties where necessary. The diagonal coefficient matrix for the Pyrogel spring layer is:

$$G_{nn}^{N2} = G_{nn}^K = k^{Pyr} \int_0^1 \int_0^1 \Phi \circ \Phi d\xi d\eta\tag{A14}$$

Again, note that $G_{nn}^{N2} = G_{nn}^K$ because the mode shape functions for the Nextel and AKK are the same. Also, the vector representing the “rigid” uni-directional foundation under the AKK is given in the same form as Eq. (8), except the modal coordinate of the AKK is used and the spring stiffness is several orders of magnitude larger than that of the Pyrogel.

Model C

The aeroelastic equations of motion for model C are nearly the same as model B, except now a static pressure differential can be imposed and the flat foundation must be replaced with the toroid.

The static pressure differential vector is:

$$P_n^{N1} = p_s \int_0^1 \int_0^1 \Phi d\xi d\eta \quad (\text{A15})$$

where p_s is the desired pressure differential. The pressure is only applied to the outermost Nextel layer.

The toroid foundation vector is given by:

$$F^K = k^{Tor} \int_0^1 \int_{\xi_1}^{\xi_2} H[-\Phi \bar{\times}_3 \vec{c}] \circ \left\{ \Lambda \bar{\times}_4 \vec{c} \right\} d\xi d\eta \quad (\text{A16})$$

where ξ_1 and ξ_2 are the dimensionless start and end locations of the toroid in the streamwise direction. Note that this term is only included in the equation of motion for the AKK.

Model D

The aeroelastic equation of motion for the single plate (SP) is:

$$M^{SP} \ddot{\vec{q}} + Z^{SP} \dot{\vec{q}} + [B^{SP} + A^{SP}] \vec{q} + S^{SP} + P^{SP} = 0 \quad (\text{A16})$$

The modal coordinate vector is now \vec{q} to avoid confusion with the individual layers in the previous models. All coefficient matrices and vector terms are the same as previous with the material properties of the single plate layer replaced where necessary.

Impulse response

To analyze impulse response in all of the theoretical models, the aerodynamic stiffness terms for the outermost Nextel layer are removed and replaced with the following vector for the hammer impulse:

$$Y_n^{N1} = F_{app} \delta(t - t_o) \Phi|_{\xi_o, \eta_o} \quad (\text{A17})$$

References

1. S. J. Hughes, F. M. Cheatwood, A. M. Calomino, and H. S. Wright, “Hypersonic Inflatable Aerodynamic Decelerator (HIAD) Technology Development Overview,” 2013.
2. S. J. Hughes, J. S. Ware, J. A. Del Corso, and R. A. Lugo, “Deployable Aeroshell Flexible Thermal Protection System Testing,” in *AIAA Aerodynamic Decelerator Systems Technology Conference and Seminar, AIAA-2009-2926*, 2009.
3. J. A. Del Corso, F. Cheatwood, W. Bruce, S. J. Hughes, and A. M. Calomino, “Advanced High-Temperature Flexible TPS for Inflatable Aerodynamic Decelerators,” in *21st AIAA Aerodynamic Decelerator Systems Technology Conference and Seminar*, vol. 1, pp. 139–161, 2011.
4. R. C. Scott, R. E. Bartels, and O. A. Kandil, “An Aeroelastic Analysis of a Thin Flexible Membrane,” in *Proc., 48th AIAA/ASME/ASCE/AHS/ASC Structures, Structural Dynamics and Materials Conference*, no. 10.2514/6.2007-2316.
5. E. H. Dowell, “Nonlinear Oscillations of a Fluttering Plate,” *AIAA Journal*, vol. 4, no. 7, pp. 1267–1275, 1966.
6. E. H. Dowell, *Aeroelasticity of Plates and Shells*. O’Reilly, 1975.
7. B. D. Goldman, E. H. Dowell, and R. C. Scott, “Flutter Analysis of the Thermal Protection Layer on the NASA HIAD,” in *Proc., 22nd AIAA Aerodynamic Decelerator Systems (ADS) Conf.*, no. 10.2514/6.2013-1254, 2013.
8. V. V. Vedenev, S. V. Guvernyuk, A. F. Zubkov, and M. E. Kolotnikov, “Experimental Observation of Single Mode Panel Flutter in Supersonic Gas Flow,” *Journal of Fluids and Structures*, vol. 26, no. 5, pp. 764–779, 2010.
9. E. H. Dowell, “Noise or Flutter or Both?,” *Journal of Sound and Vibration*, vol. 11, no. 2, pp. 159–180, 1970.
10. A. Mazaheri, “70-deg IRVE on Antares Trajectory,” tech. rep., NASA Langley Research Center, August 2013.
11. I. G. Clark, J. R. Cruz, M. F. Hughes, J. S. Ware, A. Madlangbayan, and R. D. Braun, “Aerodynamic and Aeroelastic Characteristics of a Tension Cone Inflatable Aerodynamic Decelerator,” in *AIAA Aerodynamic Decelerator Systems Technology Conference and Seminar, AIAA*, vol. 2967, p. 2009, 2009.
12. 3M, “Ceramic Textiles and Composites.” <http://www.3m.com/market/industrial/ceramics/>. [Online; accessed 19-August-2013].
13. J. Fish, Q. Yu, and K. Shek, “Computational Damage Mechanics for Composite Materials Based on Mathematical Homogenization,” *International Journal for Numerical Methods in*

Engineering, vol. 45, no. 11, pp. 1657–1679, 1999.

14. Dupont, “Kevlar Technical Guide.” http://www2.dupont.com/Kevlar/en_US/assets/downloads/KEVLAR_Technical_Guide.pdf/, 1992. [Online; accessed 19-August-2013].
15. Matweb, “DuPont Kevlar 49 Aramid Fiber.” <http://www.matweb.com/search/datasheet.aspx?matguid=77b5205f0dcc43bb8cbe6fee7d36cbb5&ckck=1/>, July 2013. [Online; accessed 19-August-2013].
16. Matweb, “MarkeTech Silica Aerogel.” <http://www.matweb.com/search/DataSheet.aspx?MatGUID=c864d25c235648d6b11711fd324b64d4&ckck=1/>, July 2013. [Online; accessed 19-August-2013].
17. J. S. Hodge and S. F. Harvin, “Test Capabilities and Recent Experiences in the NASA Langley 8-foot High Temperature Tunnel,” *AIAA Paper*, vol. 2646, 2000.
18. C. D. Kazemba, K. Tran, B. Quach, L. Kushner, A. Cassell, L. Li, R. Braun, J. D. Littell, J. van Norman, R. Johnson, *et al.*, “Determination of the Deformed Structural Shape of HIADs from Photogrammetric Wind Tunnel Data,” in *22nd AIAA Aerodynamic Decelerator Systems Technology Conference*, no. 10.2514/6.2013-1286.
19. B. W. Bader and T. G. Kolda, “Algorithm 862: MATLAB Tensor Classes for Fast Algorithm Prototyping,” *ACM Transactions on Mathematical Software (TOMS)*, vol. 32, no. 4, pp. 635–653, 2006.

REPORT DOCUMENTATION PAGE			Form Approved OMB No. 0704-0188		
<p>The public reporting burden for this collection of information is estimated to average 1 hour per response, including the time for reviewing instructions, searching existing data sources, gathering and maintaining the data needed, and completing and reviewing the collection of information. Send comments regarding this burden estimate or any other aspect of this collection of information, including suggestions for reducing this burden, to Department of Defense, Washington Headquarters Services, Directorate for Information Operations and Reports (0704-0188), 1215 Jefferson Davis Highway, Suite 1204, Arlington, VA 22202-4302. Respondents should be aware that notwithstanding any other provision of law, no person shall be subject to any penalty for failing to comply with a collection of information if it does not display a currently valid OMB control number.</p> <p>PLEASE DO NOT RETURN YOUR FORM TO THE ABOVE ADDRESS.</p>					
1. REPORT DATE (DD-MM-YYYY) 01-05 - 2014		2. REPORT TYPE Technical Memorandum		3. DATES COVERED (From - To)	
4. TITLE AND SUBTITLE Nonlinear Aeroelastic Analysis of the HIAD TPS Coupon in the NASA 8' High Temperature Tunnel: Theory and Experiment			5a. CONTRACT NUMBER		
			5b. GRANT NUMBER		
			5c. PROGRAM ELEMENT NUMBER		
6. AUTHOR(S) Goldman, Benjamin D.; Scott, Robert C.; Dowell, Earl H.			5d. PROJECT NUMBER		
			5e. TASK NUMBER		
			5f. WORK UNIT NUMBER 432938.11.01.07.43.40.08		
7. PERFORMING ORGANIZATION NAME(S) AND ADDRESS(ES) NASA Langley Research Center Hampton, VA 23681-2199			8. PERFORMING ORGANIZATION REPORT NUMBER L-20356		
9. SPONSORING/MONITORING AGENCY NAME(S) AND ADDRESS(ES) National Aeronautics and Space Administration Washington, DC 20546-0001			10. SPONSOR/MONITOR'S ACRONYM(S) NASA		
			11. SPONSOR/MONITOR'S REPORT NUMBER(S) NASA/TM-2014-218267		
12. DISTRIBUTION/AVAILABILITY STATEMENT Unclassified - Unlimited Subject Category 02 Availability: NASA CASI (443) 757-5802					
13. SUPPLEMENTARY NOTES					
14. ABSTRACT The purpose of this work is to develop a set of theoretical and experimental techniques to characterize the aeroelasticity of the thermal protection system (TPS) on the NASA Hypersonic Inatable Aerodynamic Decelerator (HIAD). A square TPS coupon experiences trailing edge oscillatory behavior during experimental testing in the 8' High Temperature Tunnel (HTT), which may indicate the presence of aeroelastic utter. Several theoretical aeroelastic models have been developed, each corresponding to a different experimental test configuration. Von Karman large deflection theory is used for the plate-like components of the TPS, along with piston theory for the aerodynamics. The constraints between the individual TPS layers and the presence of a unidirectional foundation at the back of the coupon are included by developing the necessary energy expressions and using the Rayleigh Ritz method to derive the nonlinear equations of motion. Free vibrations and limit cycle oscillations are computed and the frequencies and amplitudes are compared with accelerometer and photogrammetry data from the experiments.					
15. SUBJECT TERMS Aerodynamic brakes; Aeroelasticity; Deflection; Free vibrations; Thermal protection					
16. SECURITY CLASSIFICATION OF:			17. LIMITATION OF ABSTRACT	18. NUMBER OF PAGES	19a. NAME OF RESPONSIBLE PERSON
a. REPORT	b. ABSTRACT	c. THIS PAGE			STI Help Desk (email: help@sti.nasa.gov)
U	U	U	UU	49	19b. TELEPHONE NUMBER (Include area code) (443) 757-5802